Chalcogen controlled redox behaviour in *peri*-substituted S, Se and Te naphthalene derivatives†

Tracey L. Roemmele[a], Fergus R. Knight[b], Ellis Crawford[b], Stuart D. Robertson[c], Bela E. Bode[b]*, Michael Bühl[b]*, Alexandra M. Z. Slawin[b], J. Derek Woollins[b,d]* and René T. Boeré[a]*

Ellis Crawford   https://orcid.org/0000-0001-5511-8370

Michael Bühl   https://orcid.org/0000-0002-1095-7143

René T. Boeré   https://orcid.org/0000-0003-1855-360X

[a] Dept of Chemistry and Biochemistry and Canadian Centre for Research in Applied Fluorine Technologies, University of Lethbridge, Lethbridge, AB, T1K 3M4 (Canada)

[b] EaStCHEM School of Chemistry and Centre for Magnetic Resonance, University of St Andrews, St Andrews KY16 9ST (UK)

[c] WestCHEM, Department of Pure and Applied Chemistry, University of Strathclyde, 295 Cathedral Street, Glasgow, G1 1XL (UK)

[d] Dept of Chemistry, Khalifa University, Abu Dhabi, United Arab Emirates

† Electronic supplementary information (ESI) available: Full electronic crystal models, CCDC 2205312-2205316. For ESI and crystallographic data in CIF or other electronic format see DOI:_____

‡ Whilst logically consistent, this is not *proven*. Recourse to spectroelectrochemistry provides convincing proof by inducing EPR spectra fully consistent with 1*e* oxidation products, as described in the next section of the paper.

§ It needs to be remembered that such potentials from *electrochemically* irreversible processes are not thermodynamic data, but if the rates of electron transfer are still reasonably high, the actual potential deviations are expected to be small.

¶See Experimental-DFT Computational Methods for details.

The computed WBI for **N12**$^{2+}$ in the AA*c* conformation at 0.99 is anomalously high (Table 3); no obvious explanation could be adduced for this result.

Cyclic and square wave voltammetry of (PhE)$_2$ *peri*-disubstituted naphthalene[1,8-*cd*]dichalcoganyls and acenaphthene[5,6-diyl]dichalcoganyls (E = S,Se,Te, 12 compounds), is reported. Mixed E$_1$ = Se,Te; E$_2$=Br,I naphthalene[1,8-*cd*]halochalcoganyls were also investigated, as well as an exemplar bearing two PhS(=O) groups and another bearing one PhSe and one Ph$_2$P(=S) substituent. The voltammetry, in CH$_2$Cl$_2$/0.4 *M* [^{n}Bu$_4$N][PF$_6$] at both platinum and glassy carbon macro-disk working electrodes, shows two sequential chemically reversible and electrochemically *quasi*-reversible oxidation processes, and the lack of accessible reductions. Additional oxidations above +1.5 V vs. *Fc*$^{+/0}$ have not been investigated in detail. I*n-situ* and *ex-situ* EPR spectroscopy conclusively demonstrate that both anodic processes are 1*e* transfers; persistent radical cations could be generated for all the dichalcoganyls except when E$_1$=E$_2$=Te; for the latter case thermally stable dications are generated instead. The complex possible solution conformations of these compounds in 0, +1 and +2 charge states were modelled with DFT at the B3LYP-D3(BJ)/6-31+G(d) level of theory in a CH$_2$Cl$_2$ PCM continuum solution model and adiabatic ionisation energies calculated, which correlate linearly (R = 0.88) with the E_p^{a1} values. Crystal structures of four solvolysis and hydrolysis products of the ditellurium dications are reported and were modelled computationally. Interpretative comparisons to unsubstituted naphthalene[1,8-*cd*]dichalcogenoles are reported and the crystal structure of naphtho(1,8-*cd*)(1,2-dithiolium) tetrafluoroborate has been obtained. This is the first structure reported for any salt of this cation radical. Electron transfer mechanisms of both the (PhE)$_2$ and E$_2$ *peri*-disubstituted naphthalene series are correlated using a redox molecular orbital interpretative framework.

Introduction

There is ongoing interest in the structural, bonding and reactivity implications of main group elements placed into the *peri*-positions of polycyclic aromatic scaffolds, of which naphthalene-1,8-diyl and acenaphthene-5,6-diyl derivatives (see Chart 1) are the most common.[1-9] Pioneering work, including electrochemistry, on the naphthalene series was undertaken by Fujihara and Furukawa in the 1990's,[10,11] following on earlier work from the same group and from Glass on redox chemistry of chalcogens incorporated into aliphatic heterocycles.[12] Applications include catalysis at cationic tellurium [13] and ditellurium [14] compounds and the unique coordination environment afforded by a phosphorus bridged dinaphthalene ligand with an envelope conformation.[15] A wide variety of equivalent and non-equivalent elements, E, have been employed in the two *peri* positions, including mixed chalcogen–tin [16] and mixed halogen–chalcogen [17] functionalities at the 5,6-positions of acenaphthenes. Napthalene-1,8-disulfides are able to chelate a phosphorus atom, which can then form diphosphines which can be oxidized to stable radical cations.[18] The phosphorus-tellurium through space interactions in mixed P,Te systems have been investigated,[19] as have NMR through space spin coupling interactions in acenaphthenes substituted by -SePh and -TePh groups [20] and direct Te-Te coupling in a ditelluride.[21] Similarly, ^{77}Se NMR has been investigated for *peri*-substituted diselenides.[22] Dealkanative main-group element coupling has been reported,[23] while chelating disulfur ligands to Rh and Ir [24] and Pt have been

investigated.[25] Hypervalency and evidence for 3c/4e bonds have been extensively investigated for this class, including mixed EPh/halogen derivatives.[26]

Naphthalene and acenaphthene are attractive scaffolds for redox transformations since they have wide redox stability windows (estimated to be −3.1 *to* +1.4 V for naphthalene and −3.3 *to* +1.1 V for acenaphthene, vs Fc$^{+/0}$ in CH$_2$Cl$_2$ - see ESI for details and literature) but, unlike saturated hydrocarbons (or polyphosphazenes), are by no means inert.[27,28] The redox activity of these polycyclic aromatic hydrocarbons have their locus in the delocalized ring orbitals, with oxidation removing an electron from the π-HOMO, and reduction the addition of an electron to the π-LUMO – what we will henceforth term the *redox molecular orbitals*, RMO. Electron rich ring substituents, such as chalcogen or halogen atoms, are in principle able to modify these π-RMOs. As the data accrued in this work show, such substituents can either alter the nature and energy of the hydrocarbons RMOs (and, hence, the stability of oxidant and/or reductant), or replace them by substituent-centered ones, thereby expanding or contracting the redox ranges afforded by the native scaffolds.
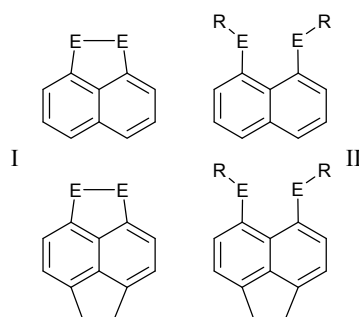

Chart 1. Two major types of chalcogen-substituted naphthalenes (top) and acenaphthenes (bottom).

The consequences for each kind of substitution motif need to be worked out in detail, as will be done here for two classes of *peri*-substituted dichalcogenides (Chart 1), namely naphthalene[1,8-*cd*] (or acenaphthene[5,6-diyl]) with and without hydrocarbon attachments, i.e. unsubstituted dichalcogenoles, **I** (E = S, Se, Te) and substituted dichalcoganyls **II** (E = S, Se, Te). Type **I** have a long history and their chemistry has been thoroughly reviewed.[29,30] Crystal structures of the whole neutral series have been reported recently.[31] They are novel electron donors in materials chemistry [32] and have been identified as strong bases in the gas phase.[33] 1,8:4,5-*Bis*(diseleno)naphthalene has been thoroughly investigated for its facile oxidation and formation of stable radical cations.[34] Soon after a complete series of chalcogen derivatives of type **I** was prepared,[35-42] the gas-phase oxidation potentials were systematically investigated using valence electron photoelectron spectroscopy (UV-PES).[43] In strong contrast, the electrochemical data for this series remains scattered and incomplete.[10,35,44-50]

The focus of this paper is a comprehensive study of the electrochemical response of the Type II compounds where R = Ph. Eighteen derivatives covering the full series of heavy chalcogens **A1 – N12** (Chart 2), some mixed chalcogen/halogen (**N13 – N16**) and a few higher oxidation state exemplars (**N17, N18**) have been studied, and their properties contrasted to the Type I derivative **N23**. We have briefly reported the

solution redox behaviour of **A1 − A3** [51] in a preliminary communication and were able to demonstrate that the measured redox potentials enabled the directed synthesis of salts of the dication **A3**$^{2+}$ (Chart 3).

	E$_1$	E$_2$		E$_1$	E$_2$		E$_1$	E$_2$
A1	S	S	**N7**	S	S	**N13**	PhSe	Br
A2	Se	Se	**N8**	Se	Se	**N14**	PhSe	I
A3	Te	Te	**N9**	Te	Te	**N15**	PhTe	Br
A4	S	Se	**N10**	S	Se	**N16**	PhTe	I
A5	S	Te	**N11**	S	Te	**N17**	Ph$_2$P(S)	PhSe
A6	Se	Te	**N12**	Se	Te	**N18**	PhS(O)	PhS(O)

N19$^+$ E = S
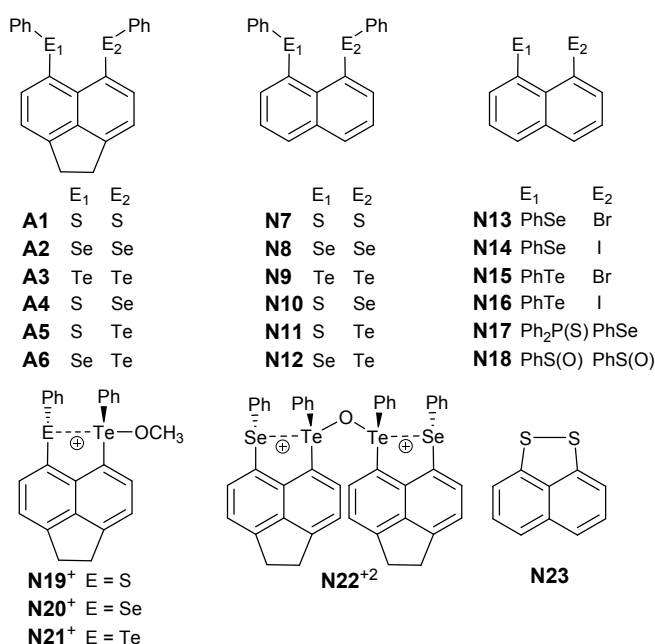**N20**$^+$ E = Se
N21$^+$ E = Te

N22^{+2}

N23

Chart 2. Structures and substituents for the investigated compounds.

This report evidently inspired others to tackle the isolation of – specifically cation radical – salts in this series. Thus far, isolation with crystal structure evidence has been adduced for salts of **N7**$^{+•}$ and **N10**$^{+•}$,[53] where the latter is actually side-by-side σ-dimerized via neighbouring Se atoms into a diamagnetic dimer [**N10**$^+$]$_2$, as well as **N8**$^{+•}$ in two forms with different counter ions; one is a diamagnetic dimer [**N8**$^+$]$_2$ similar to the previously mentioned [**N10**$^+$]$_2$ salt, whilst the other actually is the monomeric radical cation.[54] Much of this interest in isolation of the radical cations appears to be on two-center/three-electron hemi-bonds.[55-57] The focus of this article, however, is on understanding the fundamental redox responses of the neutral precursors, which will always be the primary focus of materials applications – because they are stable, easily synthesized and purified compounds. The results show that the redox responses of the Type I and II species are intrinsically complimentary, and that the identities of the chalcogen atoms E is the primary differentiator in relative redox behaviours within each series.
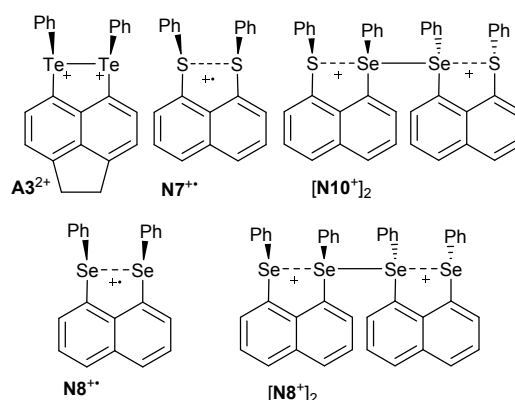

Chart 3. Structures of isolated radical cations and dications of **A1 − N18**. CSD Refcodes (the Cambridge Structural Database, release 2022.2.0)[52] for the salt structures are **A3**$^{2+}$ = ZIDHUR & ZIDJAZ;[51] **N7**$^{+•}$ = EQUTIW;[54] [**N10**$^+$]$_2$ = DUPRAJ;[53] **N8**$^{+•}$ = DUPREN;[53] [**N8**$^+$]$_2$ = EQUTES.[54]

Results

Voltammetry of the compounds. All compounds (Chart 2) were sufficiently soluble in CH_2Cl_2 to give clear to yellow-coloured solutions at analytical concentrations in 0.4 M $[^nBu_4N][PF_6]$. In each case there were between one and three oxidation processes evident and no reduction processes up to the solvent electrolyte limit (−2.4 V) except for **N18**. Broadly similar behavior was seen for all the *peri*-compounds with two PhE substituents, **A1** − **N12** (Table 1; E = S, Se, Te), using both the glassy carbon (GC) and platinum (Pt) working electrodes and from both square wave voltammetry (SWV) and cyclic voltammetry (CV). The more diverse set of compounds **N13** − **N18** was also investigated to explore and contrast the redox behaviour in (i) mixed PhE/halogen species (**N13** − **N16**) and (ii) higher oxidation state substituents (**N17**, **N18**).
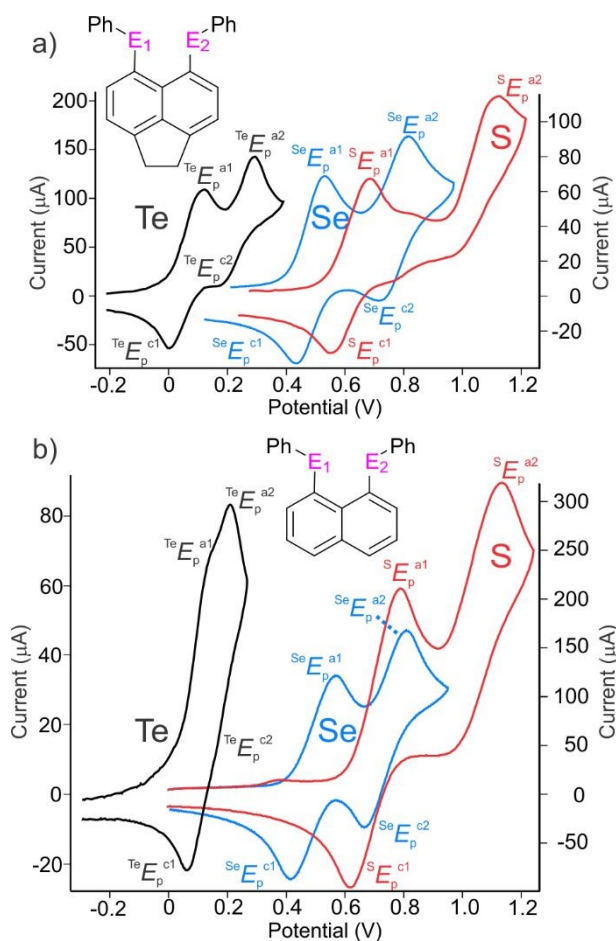

Fig. 1. Comparative CVs of: (a) 5.4 mM **A3** (black line; lhs current axis), 2.7 mM **A2** (blue line; rhs current axis), 5.5 mM **A1** (red line; lhs current axis). (b) 3.0 mM **N9**, (black line, lhs current axis); 6.6 mM **N8** (blue line; rhs current axis); 10.2 mM **N7** (red line, rhs current axis). Conditions: CH_2Cl_2 (0.4 M $[^nBu_4N][PF_6]$), ν = 0.2 V s^{-1}; T = 21.8 − 22.4 °C; at GC electrodes; potentials corrected to the Fc$^{+/0}$ scale with internal referencing.

Figs. **1a** (5,6-acenaphthene series) and **1b** (1,8-naphthalene series) show the behaviour of the *peri*-substituted di(phenylchalcogenide) compounds in CV, as also corroborated by SWV, consistent with two sequential 1e transfers.‡ At higher potentials, all species develop additional, fully chemically irreversible, oxidation processes above about +1.5 V vs. *Fc*$^{+/0}$, which have not been further investigated. We have reported on the voltammetry of **A1** − **A3** in brief in a prior communication,[51] whilst in the case of **N9**, (Fig. 1b-black line), an old communication claimed one reversible (2e) oxidation at +0.16 V vs. Ag/AgCl in 0.1 M

NaClO$_4$/CH$_3$CN at a GC electrode.[11] This reported potential is a reasonable match to our E_p^{a1} value after allowing for differences in solvent, electrolyte and reference system,[58] but our results clearly show the two step process and at best *quasi*-reversibility for the electron transfers. Curiously, these workers also claim a single reversible oxidation in solution for the dimethyl (rather than diphenyl) analogue of **N8** (+0.48 V vs. Ag/AgCl in 0.1 M NaClO$_4$/CH$_3$CN at a GC electrode), for which the potential is in good agreement for E_m^1 in **N8**, but for which a second process should be easily observable.[10] It is precisely to address such scattered and incomplete data that we were motivated to undertake the comparative study reported here.

Fig. 1 is illustrative of the behaviour of the compounds in voltammetry. First, there is an underlying basic similarity in the anodic responses of this series of *peri*-substituted naphthalene derivatives, but there is also a great deal of variation in specifics with differences in the chalcogen and in whether the 4,5-positions are occupied by H in the naphthalene or by the bridging -CH$_2$CH$_2$- atoms of the acenaphthene series. The strongest influence is clearly that of the heteroatom, with the ditellurium compounds **A3** and **N9** displaying a drastically lower onset potential for oxidation, expressed technically as the E_p^{a1} value. There is then a large jump to the onset potentials for diselenium cases **A2** and **N8**, with a smaller jump to the disulfur molecules **A1** and **N7**. When the *difference* in potentials between the first and second anodic peaks, $\Delta E_p = E_p^{a2} - E_p^{a1}$, is considered, it is immediately evident that this parameter varies as: $\Delta E_p^{S,S} \gg \Delta E_p^{Se,Se} > \Delta E_p^{Te,Te}$, and also as: $\Delta E_p^{Acen} > \Delta E_p^{Naph}$. In the latter case, evaluation of the numerical data in Table 1 indicates that lower anodic onset potentials $E_p^{a1(Acen)}$ are the main drivers for the larger ΔE_p^{Acen}, so that to a first approximation the E_p^{a2} values are independent of the 4,5-substitution.

Whereas the oxidation potentials are thermodynamic – or rather *pseudo*-thermodynamic – values, the shapes of the cathodic waves may provide insights into kinetic factors. Particularly for the diselenium and disulfur compounds (the blue and red CV waves in Fig. 1), there is an apparent difference in shapes, with, surprisingly, the disulfur cases appearing less "ideal" in CV at the 0.2 V/s scan rate shown in Fig. 1. However, a consideration of the peak shape dependence on CV scan rate is informative. The visual appearance of the 'forward' and 'reverse' waves for all six species can be interrogated by a consideration of the difference in cathodic and anodic peak potentials, i.e. $\Delta E_p^{oxid-red} = E_p^{a1} - E_p^{c1}$, often referred to as the 'peak width' and by the apparent peak currents I_p^a and I_p^c. For **A1** for the first process, $\Delta E_p^{(oxid-red)1}$ = 132 mV, and for the second, $\Delta E_p^{(oxid-red)2}$ = 148 mV, at scan rates of 0.2 V/s; at 5 V/s, those increase to 347 and 354 mV, respectively, or 2.9× and 2.4× larger. For **A2**, $\Delta E_p^{(oxid-red)1}$ = 92 mV and $\Delta E_p^{(oxid-red)2}$ = 105 mV at 0.2 V/s; at 5 V/s, those increase to 243 and 246 mV, respectively, or 2.6× and 2.3× larger. For **A3**, $\Delta E_p^{(oxid-red)1}$ = 115 mV and $\Delta E_p^{(oxid-red)2}$ = 132 mV at 0.2 V/s; at 5 V/s, those increase to 377 and 364 mV, respectively, or 3.3× and 2.8× larger. In the Napth series, peak overlap obscures the results for **N9**, but for **N7**, $\Delta E_p^{(oxid-red)1}$ = 172 mV and $\Delta E_p^{(oxid-red)2}$ = 195 mV at 0.2 V/s, versus 477 and 500 mV at 5 V/s (2.8× and 2.6×). For **N8**, 152 mV and 142 mV at 0.2 V/s, compared to 440 and 423 mV at 5 V/s (2.9× and 3.0× larger).

Chalcogen controlled redox behaviour in peri-substituted S, Se and Te naphthalene derivatives

Table 1. Cyclic Voltammetry data for compounds **A1 – N18** in CH_2Cl_2.[a]

| Cmpd, ref.	Index	Conc (mM)	Electrode	E_p^{a1} (V)	E_p^{c1} (V)	E_m^1 (V) [b]	E_p^{a2} (V)	E_p^{c2} (V)	E_m^2 (V) [c]	ΔE^{2-1} (V)	E_p^{a3} (V)	IP (eV)
A1 [59]	S S	5.4	GC	0.69	0.54	0.62	1.12	—[d]	—	0.43	1.30	5.23
			Pt	0.66	0.55	0.61	1.09	—[d]	—	0.43	1.28	5.23
A2 [59]	Se Se	5.0	GC	0.53	0.43	0.48	0.81	0.70	0.76	0.28	1.53	4.96
			Pt	0.53	0.43	0.48	0.81	0.69	0.75	0.28	1.45	4.96
A3 [59]	Te Te	5.5	GC	0.12	−0.01	0.06	0.29	0.15	0.22	0.17	1.84	4.72
			Pt	0.10	0.00	0.05	0.27	0.15	0.21	0.17	1.77	4.72
A4 [59]	S Se	2.0	GC	0.64	0.54	0.59	0.88	—	—	0.24	1.54	5.12
			Pt	0.63	0.54	0.59	0.84	—	—	0.21	1.54	5.12
A5 [59]	S Te	2.2	GC	0.44	0.28	0.36	0.85	—	—	0.41	1.45	5.05
			Pt	0.51	0.35	0.43	0.90	—	—	0.39	1.37	5.05
A6 [59]	Se Te	6.1	GC	0.29	0.15	0.22	0.73	0.51	0.62	0.44	0.93	4.91
			Pt	0.29	0.17	0.23	0.73	0.53	0.63	0.44	0.90	4.91
N7 [9]	S S	10.2	GC	0.78	0.61	0.70	1.13	0.94	1.04	0.35	1.54	5.22
			Pt	0.77	0.61	0.69	1.09	0.93	1.01	0.32	1.48	5.22
N8 [7,60]	Se Se	6.6	GC	0.57	0.41	0.49	0.81	0.66	0.73	0.24	1.49	4.99
			Pt	0.55	0.43	0.49	0.78	0.67	0.73	0.23	1.49	4.99
N9 [11]	Te Te	3.0	GC	0.16	0.07	0.12	0.21	—	—	0.05	—	4.77
			Pt	0.15	0.07	0.11	0.20	—	—	0.05	—	4.77
N10 [62]	S Se	3.7	GC	0.66	0.52	0.59	0.76	—	—	0.10	1.45	5.14
			Pt	0.65	0.52	0.59	0.80	—	—	0.15	1.56	5.14
N11 [62]	S Te	3.8	GC	0.45	0.09	0.27	0.66	—	—	0.21	1.11	5.08
			Pt	0.40	—	—	0.58	—	—	0.18	0.97	5.08
N12 [62]	Se Te	8.1	GC	0.38	0.12	0.25	0.55	0.45	0.50	0.17	0.73	4.95
			Pt	0.48	—	—	0.66	—	—	0.18	1.46	4.95
N13 [63]	Se Br	42.4	GC	1.19	0.77	0.98	1.83	—	—	0.64	—	5.62
			Pt	1.11	0.79	0.95	1.67	—	—	0.56	—	5.62
N14 [63]	Se I	12.1	GC	0.99	0.74	0.87	1.40	—	—	0.41	—	5.53
			Pt	0.94	0.76	0.85	1.28	—	—	0.34	—	5.53
N15 [63]	Te Br	5.3	GC	0.52	—	—	0.67	—	—	0.15	—	5.50
			Pt	0.74	—	—	0.88	—	—	0.14	—	5.50
N16 [63]	Te I	6.1	GC	0.66	0.48 [e]	0.57	~.95	—	—	0.29	1.63	5.37
			Pt	0.58	0.35 [f]	0.47	~0.6	—	—	<0.2	1.33	5.37
N17 [64]	Se	4.1	GC	0.90	IRR	—	1.02	—	—	0.12	—	5.26
	SPPh$_2$		Pt	0.92	—	—	1.04	—	—	0.12	1.47	5.29
N18 [64]	SO	2.8	GC	1.44 [g]	—	—	—	—	—	—	—	6.17
	SO		Pt	1.53	—	—	—	—	—	—	—	6.17

[a] Using 0.4 M [^{n}Bu$_4$N][PF$_6$] supporting electrolyte, all potentials quoted versus Fc$^{0/+}$. [b] $E_m = [E_p^a + E_p^c]/2 \approx E^{0/}$. [c] Obtained from B3LYP-D3(BJ)/6-31+G(d)/PCM(CH_2Cl_2) DFT calculations on optimized geometries of the neutral and cation radicals, see text. [d] A return wave appears at at ν = 10 V s^{-1}. [e] A second return wave appears at −0.34 V. [f] A second return wave appears at −0.02 V. [g] An IRR Red E_p^{c3} at −1.3 V.

For all five compounds with available data, the ratios of the anodic and cathodic peak currents are close to 1:1 at 0.2 V/s, and this situation does not change dramatically up to scan rates of 5 V/s, while the peak widths

7

increase about three-fold at the faster scan rate. The overall responses are classic examples in CV for two consecutive *chemically* reversible electron transfer processes, but which are all *electrochemically quasi*-reversible, indicative of significantly slowed rates of electron transfer. Based on the peak widths, these rates decrease in the sequence **N7** < **N8** and **A1** < **A2** < **A3**. For solution-phase interfacial voltammetry of molecular species of this kind, the most common causes of such slowed rates of electron transfer are higher barriers to electron transfer induced by conformational changes. If this applies here, *all* these molecules are affected by such changes, but the effects appear to be the largest for the disulfur and smallest for diselenium cases. The redox responses may be compared to a recent report on the voltammetry of simple $(ArylE)_2$ derivatives.[65]

For the mixed PhE/halogen derivatives **N13** − **N16**, the basic behaviour parallels that of the diPhE compounds, but the voltammetry is less well defined, especially for the second oxidations. There are decreasing peak separations for the two processes with increasing heteroatom size, such that for the PhTe/I case **N16** the peaks merge together much like for **N3**. Similarly, the mixed $Ph_2P{=}S$/PhSe species **N17**, has a very small peak separation between the first and second oxidation processes, while for the S(IV) compound **N18**, any attempt to distinguish a possible second oxidation peak is rendered difficult by the high oxidation potential, and the nearness to the solvent background limit. A final note regarding the voltammetric behaviour is the consistent absence of cathodic redox processes for this system, up to the solvent limits of about −2.5 V. In this, the *peri*-substituted compounds **A1** − **N17** behave similarly to naphthalene itself, for which the estimated first reduction of −3.1 V vs. $Fc^{+/0}$ (in CH_3CN solution) would not be observable below the solvent cut-off in CH_2Cl_2.[66] In this they are also in stark contrast to the Type **I** naphtho[1,8-*cd*]-1,2-dichalcogenoles, which for all cases where data is available undergo irreversible $2e$ reductions at accessible potentials, such as −1.36 V in CH_3CN for **N23**.[49]

Electron Paramagnetic Resonance (EPR) spectroscopy. As a first step in confirming the electron transfer mechanisms, EPR spectroscopy was undertaken for representative compounds that show a distinct separation between the first and second waves in voltammetry. Both chemical and electrochemical methods were used to generate the radical cations. Simultaneous electrochemical/electron paramagnetic resonance (SEEPR) spectroscopy experiments (see Experimental for details) were initially employed to generate radicals *in situ* from oxidations of **N7** − **N12**; typical results for **N7**, **N8** and **N10** are shown in Fig. 2.
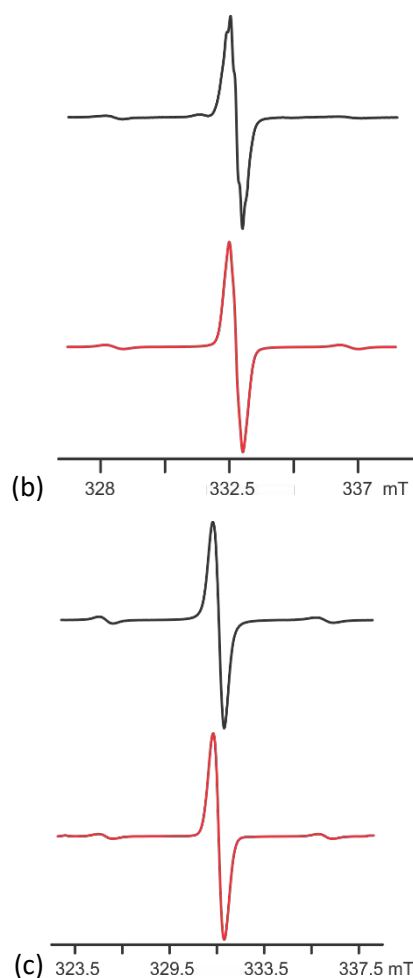

(a) 332.8   333.55   334.3   335.05   335.8 mT
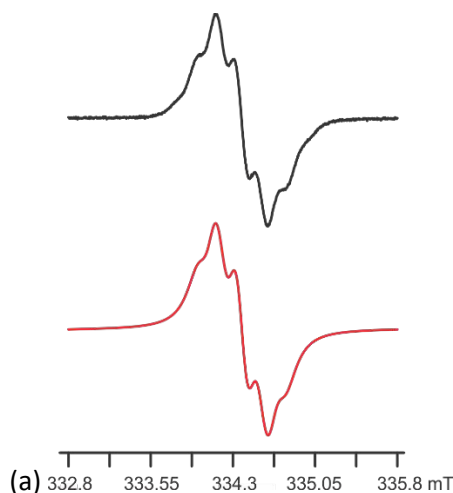
Fig. 2. SEEPR spectra (in black) obtained in CH_2Cl_2/0.1 M [$^nBu_4N$][PF_6] with an *in situ* EPR electrochemical cell. Spectra are from single scans through the indicated field ranges, while electrolysis is undertaken on (a) **N7**, (b) **N10** and (c) **N8**. Simulations with line-fitting were undertaken with WinSim2000 (in red).[67]

In the electrochemical oxidation of **N7** at voltages corresponding to $E_p{}^{a1}$ (Table 1), hyperfine splitting (HFS) is observed for ^1H nuclei on the aromatic rings, consistent with the generation of **N7$^{+\bullet}$**. For oxidations at E_p^{a1} for **N10**, the presence of Se is further indicated by the appearance of an EPR 'satellite' signal from the ^{77}Se isotope that is present at 7.63(16) % natural abundance, in addition to the central signal. The latter shows some evidence for residual splitting from aromatic ^1H nuclei, but as is common for free-radicals containing Se, general line broadening that is attributed to spin-orbit effects of the heavier chalcogen is observed; this almost obscures the super-hyperfine structure. The integrated intensity for the two satellite signals in the spectrum shown in Fig. 2b is 7.8% of the total intensity, in excellent agreement with the natural abundance of ^{77}Se. For oxidations at $E_p{}^{a1}$ of **N8**, a signal with similar ^{77}Se satellites is observed, but the central line is now so broad as to obscure any coupling to ^1H nuclei. In the spectrum shown in Fig. 2c, the two satellite signals correspond to radicals that contain *one* ^{77}Se isotope only (the spectrum is slightly too narrow to observe the minor triplet from the *two* ^{77}Se-containing radicals).[51] The theoretical relative intensity for these signals is 14.2% ($^{77}SeSe$ + $Se^{77}Se$) and the experimental integration is 12.5%, also a good agreement with theory and strong corroboration that the signal belongs to **N8$^{+\bullet}$**. The observation of these EPR spectra during electrolysis provides a powerful confirmation that the tabulated E_p^{a1} are due to 1e transfer processes,

because the spectra are fully consistent with the expected **N7**$^{+\bullet}$, **N8**$^{+\bullet}$ or **N10**$^{+\bullet}$ radical cations. Furthermore, the similar current densities found in each CV (Fig. 1) for the first and second redox process is sufficient to conclude that the second step also involves 1e transfer, whereupon **N7**$^{+2}$, **N8**$^{+2}$ or **N10**$^{+2}$ are produced.
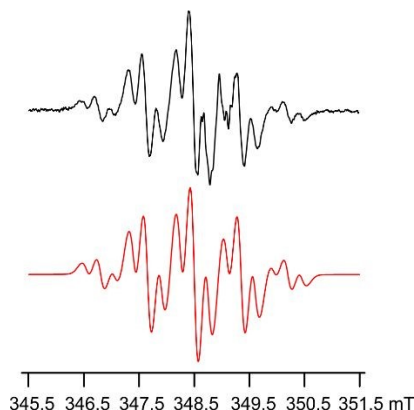

Fig. 3. Top: EPR spectrum of **A1**$^{+\bullet}$ obtained in CH_2Cl_2 by oxidation with $NOBF_4$ (from 100 accumulated scans through the indicated field range). Bottom: Simulation undertaken with WinSim2000 (in red).[67]

In the case of the acenaphthene derivatives **A1** – **A6**, chemical oxidations were performed in connection with attempts to isolate salts of the products. No EPR signals could be detected for the cation radicals of **A3** in CH_2Cl_2 using $AgBF_4$ or AgOTf, consistent with the observations that oxidation led smoothly to the formation of stable salts of **A3**$^{+2}$(X$^-$)$_2$. This also nicely explains the lack of signals in SEEPR experiments slightly positive of E_p^{a1} for **N9**.[51] These observations fit well with the expected oxidation potential of Ag$^+$ in CH_2Cl_2 of +0.65 V vs. Fc$^{+/0}$ w.r.t. the very low E_p^{a2} values for the two ditellurium species (Table 1).[58] However, for the remainder of the acenaphthene series, only Ag(I) coordination complexes could be isolated from attempted oxidation reactions.[51] We therefore used the stronger, and metal free, chemical oxidant $NOBF_4$ (+1.00 V vs. Fc$^{+/0}$),[58] added to solutions of the neutral compounds in a glove box and rapidly transferred to the resonant cavity of the EPR spectrometer. This generated strong EPR signals that are comparable with those generated by SEEPR for 1e oxidations of **N7** – **N10**. The spectrum for **A1**$^{+\bullet}$ (Fig. 3) is particularly interesting. It can be simulated as a (larger) pentet of (smaller) triplets, which are well resolved with much larger HFS than observed for **N7**$^{+\bullet}$, consistent with generation of a radical that has significant spin density on four equivalent I = ½ nuclei, which can here only be ^{1}H. The out-of-plane protons of the bridging -CH_2CH_2- component of the acenaphthene ring are thus clearly identified. The smaller HFS causing the triplets is attributed to two equivalent ring ^{1}H nuclei, which are identified as those *ortho* to the E in the $C_{10}H_4$ ring via DFT calculations on **A1**$^{+\bullet}$. The spectrum of **A2**$^{+\bullet}$ was previously reported and contains both the doublet satellite (containing one ^{77}Se) and smaller triplet satellite signal from radicals where both are ^{77}Se isotopes.[51] The EPR parameters from all experiments are compiled in Table 2, which indicates *inter alia* the considerable variation in the size of the HFS constants to ^{77}Se in different radicals. Similar oxidations with $NOBF_4$ have confirmed the EPR signals for the radical cations generated from **A4**, **A5** and **A6**, with expected characteristics. Thus, only in the cases of the ditelluro compounds **A3** and **N9**, was a radical cation not observable on the EPR timescale, fully consistent with the voltammetric data (Fig. 1 and Table 1) that the first

and second electron transfer processes are too close to enable the observation of bulk cation radicals, as also corroborated by the facile isolation of salts of dications in the case of **A3**$^{2+}$.[51] The *g*-values are found in the order **A1** < **A4** < **A5,6** < **A2**, and separately **N7** < **N10** < **N8**. Largely, these are in the expected sequence for increased spin-orbit coupling with the heavier chalcogen [34] and may be compared with data for the Type I radicals 1,2-$C_{10}H_6E_2^{+\bullet}$, where, *g*(SS) < *g*(SSe) < *g*(STe) < *g*(SeSe) < *g*(SeTe); i.e. an identical sequence except for **A6**$^{+\bullet}$.[43]

Table 2. Experimental EPR spectroscopic data ^{a}

Param	A1$^{+\bullet\,b}$	A2$^{+\bullet\,c}$	A4$^{+\bullet\,d}$	A5$^{+\bullet\,e,g}$	A6$^{+\bullet\,f,g}$	N7$^{+\bullet\,b}$	N8$^{+\bullet\,c}$	N10$^{+\bullet\,d}$
E_1/E_2	S/S	Se/Se	S/Se	S/Te	Se/Te	S/S	Se/Se	S/Se
g	2.0023(5)	2.0290(5)	2.0133(5)	2.0262(5)	2.0268(5)	2.0075(3)	2.0243(3)	2.0177(3)
$A(^{77}Se)$, MHz	—	245(3)	~156	—	254(3)	—	262(1)	232(1)
$A(^1H)$, MHz	23.8 (x 4)	—	—	—	—	5.59 (x 2)	—	4.66 (x 2)
$A(^1H)$, MHz	7.1 (x 2)	—	—	—	—	4.32 (x 2)	—	4.50 (x 2)
$A(^1H)$, MHz	—	—	—	—	—	0.22 (x 4)	—	0.33 (x 4)
LW, mT	0.10	0.6	0.57	0.54	0.46	0.13	0.48	0.31
LS, %Lorentzian	24		34	44	84	89		70

^{a} Generated for **A1** – **A6** by chemical oxidation and for **N7** – **N10** by SEEPR, in CH_2Cl_2. ^{b} 2.0086 in 1,8-$C_{10}H_6S_2^{+\bullet}$. ^{c} 2.0397 in 1,8-$C_{10}H_6Se_2^{+\bullet}$. ^{d} 2.0209 in 1,8-$C_{10}H_6SSe^{+\bullet}$. ^{e} 2.0318 in 1,8-$C_{10}H_6STe^{+\bullet}$. ^{f} 2.0409 in 1,8-$C_{10}H_6SeTe^{+\bullet}$. ^{g} $A(^{125}Te)$ satellites could also not be detected; *see* Ref, 43 for 1,8-$C_{10}H_6E_2^{+\bullet}$ data.

Analysis of the first one-electron oxidation wave.

In view of variable CV responses of the 18 compounds, we have chosen the comparative analysis on the first anodic peak potential E_p^{a1} rather than the midpoint potentials E_m (both listed, where available, in Table 1). This enables the most reliable comparisons across reversible, *quasi*-reversible and irreversible processes.§ We now set out to investigate causes for these observations and in doing so will also consider what effects are induced in the case of *mixed chalcogens*, $E_1 \neq E_2$ (**A4** – **A6** and **N10** – **N12**) and in the mixed chalcogen-halogen compounds **N13** – **N16**. For the mixed chalcogens there are two limiting cases: first, that the E_p^{a1} values are dominated by the oxidation potential of the *heavier* chalcogen in each case – indicative of localized oxidation, or secondly, that the E_p^{a1} values for mixed chalcogens are convincingly intermediate between those of the corresponding analogs with two equivalent chalcogens – indicative of oxidation processes that depend on cooperative effects between the neighbouring E_1 and E_2.[59] The CV data reported in Table 1 include results measured at both Pt and GC solid electrode interfaces; these must be treated in parallel and not mixed together. Gratifyingly, the behaviour at the two solid interfacial electrodes is found to be quite similar. Fig. 4 presents bar graphs for the E_p^{a1} values at GC sorted from least to most positive value, as a function of the 1,8-*peri* E_2/EX and ring (*N* for naphthalene, *A* for 5,6-acenaphthene) type.
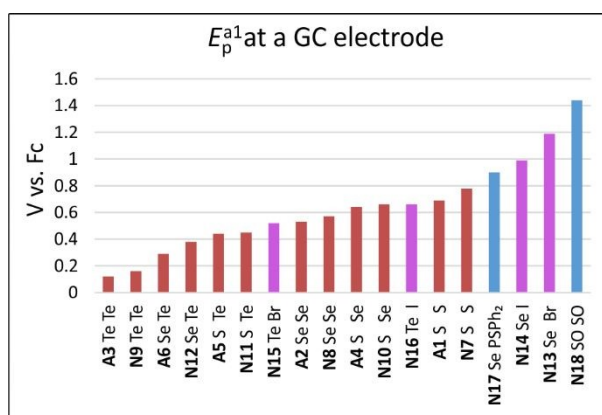
Chalcogen controlled redox behaviour in peri-substituted S, Se and Te naphthalene derivatives

Fig. 4. Bar graphs showing the large increase in E_p^{a1} values found for **A1 – N18** as a function of E/X groups measured at a GC electrode interface. (For data measured at a Pt electrode, see ESI).

The sequence and voltage increases are almost identical at the two different electrode interfaces. In the case of **A1 – N12** (red bars in Fig. 4) there is a systematic alternation of the *same* EPh groups on acenaphthene (more easily oxidized) and naphthalene (more difficult to oxidize) rings. The *average* change with ring type is 0.05 V but the standard deviation is large. The heavier the chalcogen, the lower this first oxidation potential always is. What is evident from the potentials (heights of the bars in Fig. 4) is that there is a smooth trend from the heaviest **A3**, **N9** to the lightest chalcogens **A1**, **N7** that is *not* determined by the identity of the heavier chalcogen in mixed E,E' compounds (**A4 – A6**, **N10 – N12**). This indicates that the potentials are determined cooperatively. It is also important to recognize how wide the potential range is, from a low of +0.12 V for **A3** to a high of +1.44 V vs. Fc$^{+/0}$ for **N18**. The facile oxidation potential of **N9** was already recognized in early work by Fujihara et al.[11]

DFT Calculations. In a search for causation of the trends in E_p^{a1} values, the published crystal structures for this series were consulted, and the amount by which the E···E distances are *less than* the sums of the van der Waals radii of two atoms was used as a proxy for the degree of *peri* interaction (and hence of HOMO destabilization). The results of this search is presented in ESI; though quite successful, this failed to harmonize all the compounds into a unified whole and instead we turn to full geometry optimizations via DFT computational chemistry of the three charge states for all species observed in voltammetry.[59,62,63] ¶ The differences in energies can be used to compute adiabatic ionisation potentials (AIP), which are the appropriate values for comparison to solution voltammetry in view of the relatively long time-scales. In early stages of this work, the vertical ionisation potentials (VIP) were also computed, but it could easily be demonstrated that parabolic rather than linear fits occur (Fig. S25 in the ESI); VIP is by contrast the appropriate parameter to use for correlations of UV-PES data.

A wide range of possible conformations have been encountered, or considered computationally, amongst the different *peri*-substituted phenylchalcogenides **A1 – N12** over the three charge states, 36 species in all. The definitions and labels employed for these conformations, using a widely adopted approach, are depicted in Scheme 1;[2,7,59,62,63] this scheme can also be used for **N13 – N16**, the halo-derivatives, by replacement of one PhE group by X = Br or I, thereby reducing the number of possible conformers.[62]

Geometries were defined as follows; each of the phenyl rings could be (independently) located perpendicular to the plane of the aromatic structure (A), parallel to the plane (B) or between these two extremes (C). A "C" classification was bestowed upon geometries which had a C11 – E1 – E2' angle of between 120° and 160°. Lower case "c" and "t" define the phenyl rings as being either *cis* or *trans* respectively to one another. This labelling scheme was applied to both naphthalene and acenaphthene based compounds (Scheme 1).
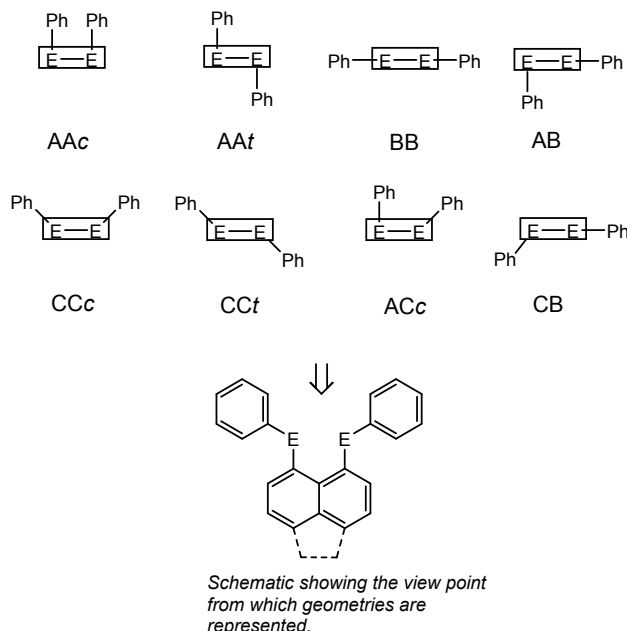
Scheme 1. Schematic depictions of conformations considered for the *peri*-substituted 1,8-naphthalene and 5,6-acenaphthene phenylchalcogenides. The rectangular box symbolises a "side-on" view of the naphthalene ring system, i.e as shown at bottom.

In our previous publication on **A1 – A3**, the DFT computed lowest energy isomers for the neutral, mono and dications were obtained using dispersion-corrected DFT along with PCM solvent models for CH_2Cl_2.[51] These calculations correctly predicted the *AAc* geometry obtained experimentally in crystal structures of **A3**$^{2+}$. A similar, exhaustive, search for conformational preferences for all three charge states of **N1 – N18** has been undertaken at similar levels of theory, in gas and condensed-phase models and with/without attempts to account for the effects of dispersion, as reported in detail in the ESI for this paper. These and additional DFT calculations (see below) give a reasonable confidence that, either the lowest energy solution conformations relevant to all compounds in this paper are as listed in Table 3, or that the difference in energy to the global minimum is small (< 10 kJ/mol). 3D plots of the optimized geometries are provided in Fig. 5 and are also provided as MDL '.MOL' files with the ESI. Important is the realization that both the inclusion of empirical dispersion (see below) and polarized continuum solvent models (PCM) are essential to reproduce several of these conformational preferences.
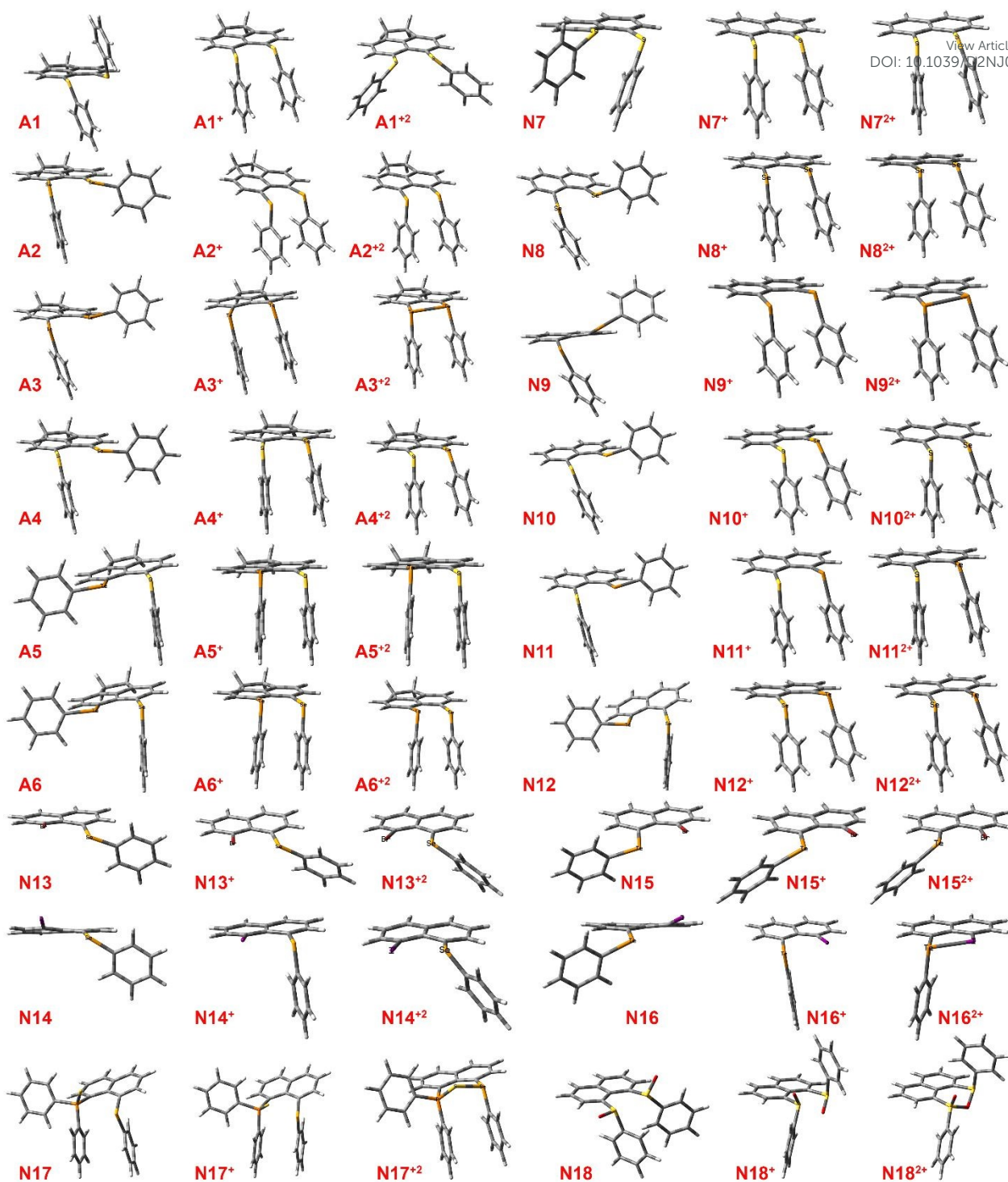
Chalcogen controlled redox behaviour in peri-substituted S, Se and Te naphthalene derivatives

Fig. 5. Representations of the optimized lowest energy geometries for neutral, radical cation and dications **A1** – **N18** at the B3LYP-D3(BJ)/6-31+G(d) level of theory in a PCM model for CH_2Cl_2. Interatomic data and comparisons to literature are provided in Table 3.

Chalcogen controlled redox behaviour in peri-substituted S, Se and Te naphthalene derivatives

Table 3. DFT Modelling of A1 to N23 in Three Charge States [a]

Comp.	Index	Neutral Conform.[b]	d(E···E)[c]	<Σr_vdW /Å[d]	% Σr_vdW[d]	Exptl/Å	WBI[e]	Monocat. Conform.[b]	d(E···E)[c]	<Σr_vdW /Å[d]	% Σr_vdW[d]	%-short.[f]	WBI[e]	Dicat. Conform.[b]	d(E···E)[c]	<Σr_vdW /Å[d]	% Σr_vdW[d]	%-short.[f]	WBI[e]
A1	S S	AAt (AB)[g]	3.291	−0.31	91.4	3.274(4), 3.288(4)	0.01	AAc (BB)[z]	2.947	−0.65	81.9	10.5	0.13	CCc	2.896	−0.70	80.4	12.0	0.19
A2	Se Se	AB[h]	3.209	−0.59	84.4	3.1834(7)	0.06	AAc	3.044	−0.76	80.1	5.1	0.18	AAc	2.659	−1.14	70.0	17.1	0.61
A3	Te Te	AB (CB)[i]	3.402	−0.72	82.6	3.367(2)	0.13	AAc	3.287	−0.83	79.8	3.3	0.22	AAc[η]	2.894 2.7960(7); 2.810(2)	−1.23	70.2	14.9	0.77
A4	S Se	AB[j]	3.122	−0.58	84.4	3.113(4)	0.06	AAc	2.998	−0.70	81.0	4.0	0.15	AAc	2.612	−1.09	70.6	16.4	0.52
A5	S Te	AB[k]	3.172	−0.69	82.2	3.158(1)	0.09	AAc	3.102	−0.76	80.4	2.2	0.17	AAc	2.707	−1.15	70.1	14.7	0.59
A6	Se Te	AB[l]	3.249	−0.71	82.0	3.248(2)	0.11	AAc	3.163	−0.80	79.9	2.7	0.20	AAc	2.767	−1.19	69.9	14.8	0.69
N7	S S	ACc (AB)[m]	3.232	−0.37	89.8	3.0044(6), 3.021(2)	0.02	AAc[α]	2.8753 2.8168(9)	−0.72	79.9	11.0	0.14	AAc	2.518	−1.08	69.9	22.1	0.46
N8	Se Se	AB[n]	3.145	−0.66	82.8	3.135(1)	0.07	AAc[β]	2.990 2.813(9), 2.9416(4)	−0.81	78.7	4.9	0.19	AAc	2.612	−1.19	68.7	17.0	0.63
N9	Te Te	AB (CCt)[o]	3.366	−0.75	81.7	3.2872(2)	0.14	AAc	3.242	−0.88	78.7	3.7	0.23	AAc	2.874	−1.25	69.8	14.6	0.77
N10	S Se	AB[p]	3.050	−0.65	82.4	3.063(2), 3.030(1)	0.03	AAc[γ]	2.933 2.813(13)	−0.77	79.3	3.8	0.16	AAc	2.553	−1.15	69.0	16.3	0.55
N11	S Te	AB[q]	3.108	−0.75	80.5	3.068(2), 3.098(1)	0.10	AAc	3.045	−0.82	78.9	2.1	0.17	AAc	2.662	−1.20	69.0	14.4	0.60
N12	Se Te	AB[r]	3.197	−0.76	80.7	3.158(2), 3.192(2)	0.12	AAc	3.114	−0.85	78.6	2.6	0.20	AAc	2.731	−1.23	69.0	14.6	0.99
N13	Se Br	B[s]	3.169	−0.56	85.0	3.1136(6)	0.05	C	3.118	−0.61	83.6	1.6	0.07	C	3.048	−0.68	81.7	3.8	0.16
N14	Se I	B[t]	3.332	−0.55	85.9	3.2524(8)	0.06	A	3.114	−0.77	80.3	6.6	0.18	C	3.016	−0.86	77.7	9.5	0.35
N15	Te Br	B[u]	3.259	−0.63	83.8	3.191(1)	0.07	C	3.200	−0.69	82.3	1.8	0.05	C	3.093	−0.80	79.5	5.1	0.22
N16	Te I	B[v]	3.417	−0.62	84.6	3.315(1)	0.09	A	3.248	−0.79	80.4	5.0	0.19	A	2.859	−1.18	70.8	16.3	0.74
N17	Se SPPh$_2$	AAc[w]	3.366	−0.33	91.0	3.3491(8)	0.03	AAc[δ]	2.877	−0.82	77.8	14.5	0.21	AAc[θ]	2.261	−1.44	61.1	32.8	0.91
N18	SO SO	ACc[x]	3.086	−0.51	85.7	3.076(2)	0.03	AAt[ε]	2.370	−0.95	71.4	(6.8)	0.14	AAt[ι]	1.736	−1.66	52.3	14.6	0.71
N23	S S	Flat[y]	2.137	−1.46	59.4	2.0878(7)	0.99	Flat[ζ]	2.086	−1.51	57.9	2.4	1.06	Flat	2.045	−1.55	56.8	3.8	1.19

[a] At the B3LYP-D3(BJ)/6-31+G(d) level of theory in a PCM model for CH$_2$Cl$_2$.¶ Only the lowest energy conformers of the varying chemical compositions are listed. Conformations defined as per Sch. 3 and Fig. 5 [b] Bold entry = SC-XRD structure known; experimental conformation listed if different; CSD refcodes given via footnotes. [c] The separation between nuclei of the *peri*-bound heteroatoms, except where noted. [d] The amount that d(E···E) is less than the sums of v.d.Waals' radii of the two atoms.[68] [e] WBI undertaken in Gaussian W16.[69] [f] Shortening of d(E···E) w.r.t. neutral conformer. [g] WARKIL.[59] [h] WARKOR.[59] [i] WARKUX.[59] [j] WARLAE.[59] [k] WARLEI.[59] [l] WARLIM.[59] [m] LUFCIY;[9] LUFCIY01.[60] [n] POPCON.[60] [o] ZODNIP.[11] [p] MUWVOQ;[62] MUWVOQ01.[2] [q] MUWVUW.[62] [r] MUWWAD.[62] [s] CIKPUI.[70] [t] CUZDOR.[63] [u] CUZDUK.[63] [v] CUZFAF.[63] [w] MUXGOC;[64] Conformation defined w.r.t. one of the two Ph rings on P; the distance here is Se to S, while d(P···Se) is shorter at 3.291 and d(P=S) = 1.317 Å. [x] MUWWIL.[62] [y] DAQMUE.[31,61] [z] GUQNOY.[71] [α] DUPREN.[53] [β] EQUTIW;[54] EQUTES;[54] GUQNUE.[71] [γ] DUPRAJ.[53] [δ] Conformation defined w.r.t. one of the two Ph rings on P; the distance here is Se to S, while d(P···Se) = 2.326 and d(P=S) = 1.172 Å. [ε] The distance listed for the monocation is d(S···O); d(S···S) = 3.157, d(S–O) = 1.561, d(S=O) = 1.507 Å. [ζ] SC-XRD is [N23]BF$_4$; this work. [η] ZIDHUR;[51] ZIDJAZ.[51] [θ] The distance here is Se to S, while d(P···Se) = 3.328 and d(P=S) = 0.969 Å. [ι] The distance listed for the dication is d(S···O); d(S···S) = 2.940, d(S=O) = 1.456 Å.

This will probably be a full-width table in the journal.

DFT modelling for neutral and oxidized A1 − N12 (upper six rows in Fig. 5). As mentioned above, neutral **A1** proves to be an exception by preferring AA*t* as the most stable conformation in the SC-XRD structure (CSD Refcode: WARKIL)[59] and is computationally also preferred but with a very small preference of +1.1 kJ/mol over AB. By contrast, neutral **N7** is more stable as AB than AA*t* by a similarly small energetic preference. Notably, all the other neutral species **A2 – N12** are computed to be most stable as AB, albeit with variations amongst slightly *cis* or *trans* relative dispositions of the two E atoms w.r.t. the mean naphthalenic ring planes. This agrees with the reported crystal structures for all species except **A3**, which crystallizes as CC*t* (CSD refcode: WARKUX).[59] Each of the observed crystal forms for the neutral species (see Table 3) has been thoroughly examined and computationally characterized in the original publications.[59,62,63] The importance of the new calculations is to provide reference points to the corresponding mono- and dioxidized ion geometries. The inter-chalcogen distances, the (low but non-zero) Wiberg bond index (WBI) values,[69] and the significantly short non-bonded contact distances d(E-E) [ranging from 0.31 to 0.76 Å $<\sum r_{vdW}$] of all the neutral species, indicate that the preferred conformations derive from the best possible responses to the uncomfortably close *peri*-distances between the electron rich chalcogen and halogen atoms. The WBI values, a measure for the covalent bond order, are certainly small but range considerably (min. 0.01, max. 0.14, mean 0.08(4)) and have been thoroughly addressed in previous publications.

Following the first oxidation event, the AB geometry which was previously the most stable conformer for **N7** and AA*t* for **A1** both change to AA*c*, which is adopted at our level of theory for **A1$^{+\bullet}$** to **N12$^{+\bullet}$** when the D3(BJ) correction for dispersion and a PCM(CH$_2$Cl$_2$) model are employed; for a greater diversity of preferences at other levels of calculation, please consult the ESI. The WBI values increase upon 1*e* oxidation to remarkably uniform values [min. 0.13, max. 0.23, mean 0.18(3)], as also do the amounts by which d(E···E) is less than $\sum r_{vdW}$ (min. -0.65, max. -0.88, mean -0.78(6) Å).

Removing a further electron again decreases the bond lengths between atoms (Table 3) and the conformations are all predicted to be (small variants on) AA*c* except for **A1^{2+}**, which adopts CC*c* with an energetic preference of 8.9 kJ/mol over AA*c*. The WBI for this CC*c* conformation is much smaller (0.194) compared to the range 0.46 – 0.77, mean = 0.62(10), for the remainder of the series.# These results are distinctly different from gas-phase DFT models that do not consider the London dispersion forces that operate between the pendant PhE rings, for which a much wider variety of geometry preferences has been found (ESI, ESI of Ref. 51).
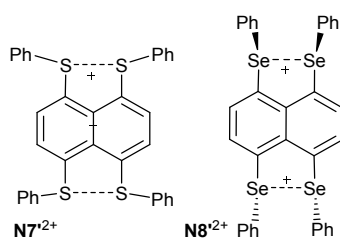

Chart 4. Differential conformations reported in salts of **N7'$^{2+}$** and **N8'$^{2+}$**.

Regarding the exceptional CC*c* conformation computed as the most stable for **A1**[2+], it is noteworthy that a closely similar conformation was obtained in the X-ray crystal structure reported for diradical-dications of 1,4,5,8-tetraPhS (**N7'**[2+] in Chart 4; CSD Refcode = GUQNOY); by contrast, the tetraselenide analogue **N8'**[2+] (CSD Refcode = GUQNUE) adopts the conventional AA*c* conformer thus far observed for all the other salts of cation radicals.[71] Nevertheless, the energy differences between these computed conformations are small and certainly lower than expected lattice energies. Hence, we cannot be certain that such differences will apply in solution voltammetry.

D3(BJ) Dispersion Correction. The importance of noncovalent interactions, and modelling them via dispersion-correction, has been noted for a series of dibenzo-1,5-dichalcogenocines.[72] Also, previous experience with pendant phenyl rings attached to small thiazyl pancake-bonded dimers has demonstrated the necessity of including corrections for dispersion in the correct modelling of strongly dimerized 5-aryl-$1\lambda^2,3\lambda^2$-dithia-2,4,6-triazines.[73] In that study, the conformations were computed using a range of popular dispersion correcting regimes [B3LYP-D3, B3LYP-D3(BJ), M062X, APFD] compared to the native B3LYP functional. Without correction, the pendant aryl ring centroid-to-centroid distances in the converged models were found to be much larger than experimental (+13.1%), whereas these corrections were all found to be much closer (-6,2, -7.3, -8.4 and -8.8%) to experiment. At the same time, *all* these methods over-corrected the attraction. Notably, the overall geometrical comparison of these dithiatriazine dimer structures was found closest to experiment using B3LYP-D3(BJ).[73] For this reason, and assuming that the pendant phenyl rings in **A1** to **N12** will display similar behaviour, we have employed the B3LYP-D3(BJ)/6-31+G(d) level of theory in the PCM(CH$_2$Cl$_2$) solvent model in this work also, while recognizing that the phenyl ring attractions are likely to be somewhat exaggerated by the Grimme D3(BJ) corrections,[74].

To monitor this phenomenon, we define the perpendicular distance d_{C-Pl} between the centroid of one of the phenyl rings in an AA*c* conformation and the least-squares plane of the second ring. There are always two different values for this parameter because of the offset 'π-stacking' arrangement between the two rings (as in the lowest-energy lattice structure for graphite with C atom over ring centroid, for which d_{C-Pl} = 3.348 Å).[75] We take the *shorter* of these two values as the significant value. In the two dication salts of **A3**, the experimental d_{C-Pl} = 3.53 Å in ZIDHUR (Chart 4), and 3.34 Å in ZIDJAZ;[51] the DFT-D3(BJ) model computes 3.31 Å for **A3**[2+]. In the monocation salt of **N7**, d_{C-Pl} = 3.32 Å in DUPREN;[53] the DFT-D3(BJ) model gives 3.25 for **N7**[+•]. In the monocation salt of **N8**, d_{C-Pl} = 3.32 Å in EQUTIW,[54] while for the dimeric dication **[N8$^+$]$_2$**, d_{C-Pl} = 3.27 Å in EQUTES;[54] the DFT-D3(BJ) model yields 3.24 for **N8**[+•]. For the dimeric dication **[N10$^+$]$_2$**, d_{C-Pl} in DUPRAJ reports an average d_{C-Pl} = 3.32(2) Å;[53] the DFT-D3(BJ) model yields 3.27. For the monocations (combinations of S, Se) the computed d_{C-Pl} using B3LYP-D3(BJ), at -1.2%, is close to but slightly smaller than experiment. For the dicationic ditellurium **A3**[2+], the distance is 16% shorter than experiment, possibly reflecting the larger $d(E\cdots E)$. Hence, it appears that D3(BJ) does over-correct for the dispersive attraction of pendant rings, just as we noted for dithiatriazine dimers.[73] Careful monitoring of the actual separation of the pendant rings (via d_{C-Pl})

and the compatibility of this spacing with the *peri*-distances and their variation by element size has been undertaken throughout.

The computational predictions of solution conformations (Fig. 5; Table 3) thus provide a reasonable basis for rationalizing the significant geometrical changes that occur on oxidizing **A1** – **N12** by one and two electrons. Notably, for six different salts for which crystal structures have been obtained (Chart 4), from four exemplars in this series (**A3**$^{2+}$, **N7**$^{+\bullet}$, **N8**$^{+\bullet}$ and **N10**$^{+\bullet}$), there is complete agreement on conformation with these solution-phase computational predictions. Particularly noteworthy from Table 3 is how large the % shortening of d(E$\cdots$E) is upon oxidation for all the Type II structures, especially for the dichalcogenides **A1** – **N12** (average of 15.7% for the dications), which is so much larger than for the Type I structure **A23** (3.8%). This amount of shortening is only possible in cases, such as the Type II molecules, where strongly repulsive non-bonded 2c4e interactions are *relieved* by the removal of electrons and the onset of bonding interactions in the resulting formal 2c3e or 2c2e bonds.

Chemical Behaviour of Oxidized Dichalcogenides. The most detailed investigation has been undertaken on isolated salts of the dications **A3**$^{2+}$, **A5**$^{2+}$ and **A6**$^{2+}$.[51] Attempted recrystallizations in dry CH_3OH resulted in methanolysis. Our evidence for these products is limited; convincing NMR data or combustion analysis was not obtained at the time of their isolation, so that we cannot comment on yields or even confirm that these were the major products (which they did appear to be). But their identity and structures are unambiguously established by single-crystal X-ray diffraction (SC-XRD). Crystal structures have been determined for three exemplars **A19** - **A21** (Fig. 6), isolated as BF_4^- salts. In **A19**, there are two independent formula units in the asymmetric unit, along with two water molecules. **A20** crystallizes with a positionally disordered BF_4^- ion and is a 1:1 methanol solvate, as also is **A21** but its anion is ordered. Most noticeably, the coordinated –OMe group is consistently found attached to Te (i.e. a preference over S or Se, when present). In one case, the isolated crystals are the product of hydrolysis, rather than methanolysis, leading to the oxo-bridged dimeric structure **A22**$^{2+}$ (isolated as crystals with two BF_4^- ions and containing about 1.7 equivalents of CH_2Cl_2 per formula unit, corresponding to slightly low occupancies over two separate sites within the asymmetric units) and here too the bridging O atom is bonded to the two Te atoms rather than to Se. A consideration of the atomic charges from natural population analysis (NPA) provides an insight to this behaviour. The two Te atoms in **A3**$^{2+}$ have NPA charges of +1.27 and +1.28; for **A5**$^{2+}$ the charge at Te is +1.45 and at S +0.65; for **A6**$^{2+}$ the charge at Te is +1.40 and at Se +0.89. The preferential bonding of O to Te implies selection of the higher charge differential, developing bonds with significant ionic character. What these results demonstrate conclusively is the very high electrophilicity of the oxidized phenylchalcogenides and their strong susceptibility to nucleophilic attack.
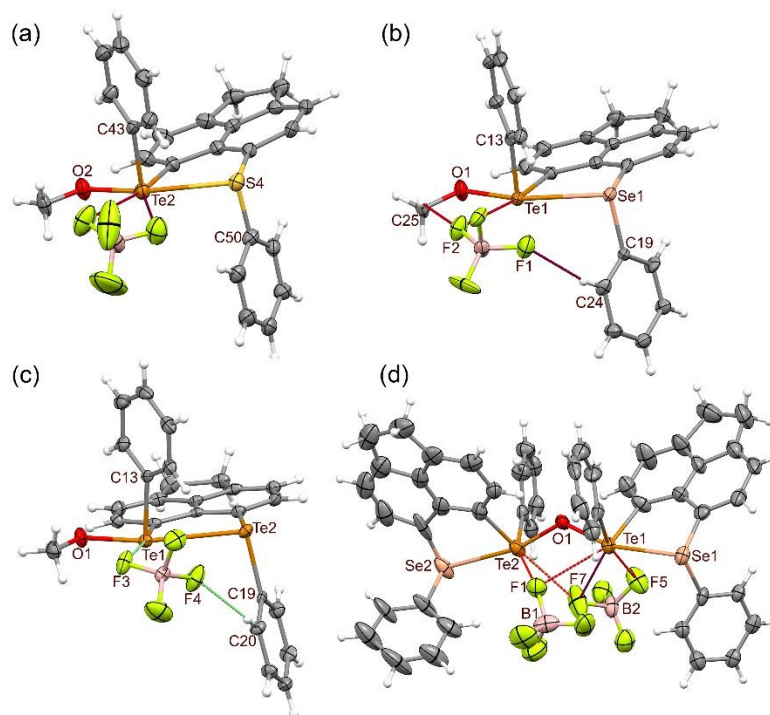
New Journal of Chemistry

Chalcogen controlled redox behaviour in peri-substituted S, Se and Te naphthalene derivatives

Fig. 6. Displacement ellipsoids plots (40% probability) of methanolate cations (a) **A19⁺**, (b) **A20⁺** and (c) **A21⁺** in their BF_4^- salts and (d) the bridged dication hydrolysis product **A22²⁺** in which putative TeOH moieties have dimerized by condensation. A second independent formula unit and both waters of crystallization are omitted from (a).

These solvolysis products of the dications **A3**, **A5** and **A6** add diversity to the already substantial list of derivatives of the Type II *peri*-substituted dichalcogenides.[7,9,11,59,62-64,76,77] Key geometrical parameters from both the SC-XRD and from B3LYP-D3(BJ)/6-31+G(d)/PCM(DCM) calculations are listed in Table 4. Noticeably, all four structures show *quasi*-linear, cationic structures with the methoxy (or oxo in **A22**) group in the linear position and thereby approximately coplanar with the acenaphthene rings. The disposition of the phenyl groups attached via E is found, unusually for this study, to be *trans*, generating an AA*t* geometry (w.r.t. the PhE substituents). Similar *trans quasi*-linear structures are reported for methylated cations (as triflate salts, CSD refcodes: REKPOO, CH₃-PhTe-PhS; REKPUU, CH₃-PhTe-PhSe; REKPEE, CH₃-PhTe-PhTe; see Chart 5).[76] Whilst these have substantially the same conformations as found in the cations of **A19** – **A22**, their d(Te···E′) are all 7.3 – 12% longer and, correspondingly, have % $\sum r_{vdW}$ that are 81-84%, compared to 74-75% in the solvolysis structures. Compared to these methylated cations, the usual metrics at the PAH scaffold (splay angles, out-of-plane distortions of E, bay region angles and central torsion angles for the acenaphthene rings) show lower distortions in the cations of **A19** – **A22**, consistent with the shorter *peri*-distances. A possible explanation for these shorter distances is the higher electronegativity of the oxygen substituents: if thereby the (R)O–Te entities are more electropositive, a stronger dative bond from the E(II) donor may be induced. Support for this notion comes from oxidation by halogens, although direct comparators do not exist, because iodine does not form such structures and bromine with other chalcogen combinations affords E(IV)Br₂/E(II) covalent adducts that adopt quite different structures. Nevertheless, in the cationic bromo adducts of the related PhSe/PhS and PhSe/PhSe systems (which are known for both the naphthalene and acenaphthene series –

see Chart 5 for the structures and CSD refcodes). Curiously, these four species are all found in the AA*c* conformation independent of variations in their splay angles, but they have % $\sum r_{vdW}$ of 73-74%. When DFT modelling of these solvolysis products was undertaken (Table 4), it was possible to reproduce the AA*t* cation structures found in the SC-XRD quite well, but in each case, the alternate AA*c* geometry could also be minimized and was always found to be 9 – 12 kJ/mol more stable, when using the standard B3LYP-D3(BJ)/6-31+G(d)/PCM(DCM) method adopted in this work. This conformation reversal could also be due to the overcorrection for Ph/Ph ring attraction from using the D3(BJ) method (see above). Indeed, the computed WBI for both the Te–E' and Te–O bonds are slightly higher in each case in the AA*t* conformers.

Table 4. Crystallographic and DFT Computed Structure Parameters for Solvolysis Products

Compound	A19	A19[a]	A20	A21	A22	A22[b]
Peri moieties	S/TeOMe-1	S/TeOMe-2	Se/TeOMe	Te/TeOMe	Se/TeOTe-1	Se/TeOTe-2
SC-XRD						
d(Te⋯E'), Å	2.905(3)	2.901(3)	2.960(2)	3.0769(9)	2.932(2)	2.979(6)
% $\sum r_{vdW}$[c]	75.2	75.2	74.8	74.7	74.3	74.9
WBI (Xray)	0.26	0.26	0.34	0.42	0.36, 0.38	—
d(Te-O), Å	1.91(1)	1.978(9)	1.960(6)	1.990(3)	1.971(6)	1.973(6)
% $\sum r_{cov}$[d]	93.8	95.2	94.4	95.7	94.9	95.0
∠E'-Te-O, °	167.2(2)	165.7(2)	166.4(3)	167.9(1)	162.8(2)	163.2(2)
∠Te1-C1-C10, °	121.0(7)	119.2(7)	120.4(7)	122.7(3)	121.4(8)	126(1)
∠C1-C10-C9, °	128.3(9)	129.4(9)	132.1(9)	130.5(4)	128.1(9)	127(2)
∠E'-C9-C10, °	119.4(7)	119.4(7)	118.0(7)	119.8(3)	120.4(8)	117(1)
Splay angle, °	8.7	8.0	10.5	13.0	9.9	10
O-o-p Te, °	0.085	0.197	0.041	0.005	0.290	0.221
O-o-p E', °	−0.158	−0.266	−0.218	0.127	−0.136	−0.241
C6-5-10-1, °	−177.7(9)	178.7(9)	179.4(9)	179.0(4)	178(1)	178(2)
C4-5-10-9, °	180(1)	−179.0(9)	−180(1)	−179.9(4)	−175(1)	−180(2)
CH$_3$ Refcode[e]	REKPOO	REKPOO	REKPUU	REKPEE	REKPUU	REKPUU
DFT calculations[f]						
DFT(AA*c*), kJ/mol[g]	−9.0	—	−7.4	−7.4	−15.1[g]	—
$d_{TeE'}$(AA*t*, AA*c*), Å	2.896, 2.940	—	2.972, 3.019	3.111, 3.159	2.938, 2.984[g]	—
WBI (AA*t*, AA*c*)	0.28, 0.26	—	0.34, 0.35	0.41, 0.39	0.38, 0.36[g]	—
d_{C-Pl} in AA*c*, Å[h]	3.320	—	3.318	3.310	3.333[g]	—
d_{TeO}(AA*t*, AA*c*), Å	2.001, 2.008	—	2.013, 2.020	2.032, 2.036	2.001, 2.014[g]	—
WBI (AA*t*, AA*c*)	0.61, 0.59	—	0.58, 0.57	0.55, 0.54	0.53, 0.52	—

[a] Second molecule, since Z'=2. [b] Second half of molecule bridged by –O–. [c] Fraction = d(Te⋯E')/(r_{vdW}Te+r_{vdW}E'). [d] Fraction = d(Te⋯O)/(r_{cov}Te+r_{cov}O). [e] I.e. for crystal structures of salts containing the methylated monocations of the corresponding Type II compounds. [f] B3LYP-D3(BJ)/6-31+G(d)/PCM(CH$_2$Cl$_2$) optimization with 0 imaginary frequencies in two conformations, AA*t* and AA*c*. [g] All four crystal structures are found in the AA*t* conformation, but DFT favours AA*c* by this amount of energy. [h] The shorter of two distances, each from the ring centroid of one Ph ring to the mean plane of the second Ph ring in the AA*c* conformation. [g] Both the AA*c* and AA*t* conformers were constrained to C_2 point group symmetry, to save computational time; the differences in energy to unconstrained models are found to be <0.5 kJ/mol.
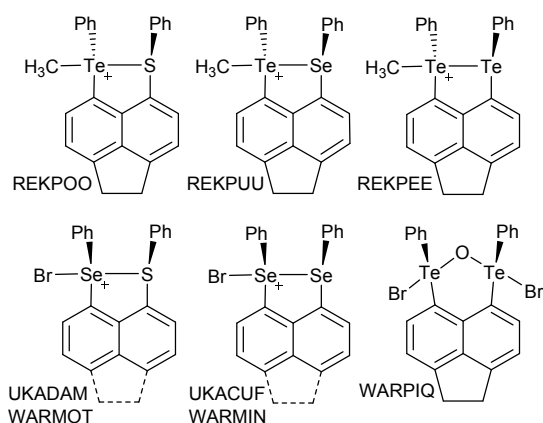
Chart 5. Comparison structures for solvolysis reaction products, with CSD refcodes.[26,76,77]

Of interest to the oxo-bridged hydrolysis structure **A22** is the report that hydrolysis also occurs from attempts to oxidize **A3** with Br_2, even in dry CH_2Cl_2 solutions, leading to the neutral C_3Te_2O ring-structure mentioned previously with CSD Refcode WARPIQ (Chart 5), in which the oxygen atom is ring-forming across the *peri*-gap, rather than bridging between cations.[64]
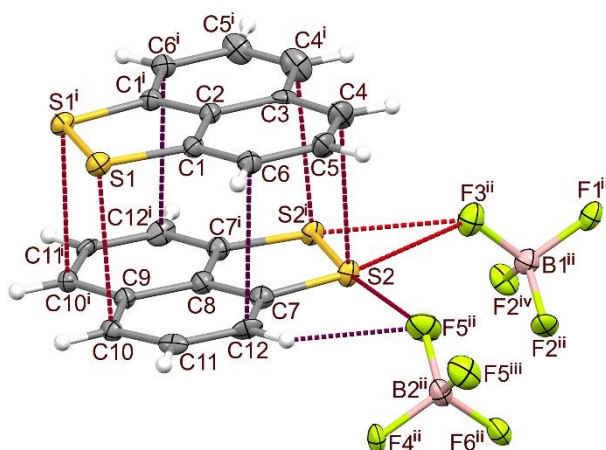

Fig. 7. Displacement ellipsoids plot (40% probability) of naphtho[1,8-*cd*]-1,2-dithiolium tetrafluoroborate [**N23**]BF$_4$, showing one of three crystallographically independent pancake-bonded cation dimers and two associated anions. The cations and one anion crystallize at a mirror plane through the C2,C3,C8,C9 and B1 atoms; sym. oper.: [i] -x, y, z; [ii] x, 1+y, z; [iii] 1-x, 1+y, z; [iv] -x, 1+y, z. Intermolecular contacts shorter than (r_{vdW} − 0.2) Å are shown by coloured dashed lines (shortest orange; longest blue-purple).

Isolation and Crystal Structure of naphtho(1,8-*cd*)(1,2-dithiolium) tetrafluoroborate.

Crystals of [**N23**]BF$_4$ were obtained by electrocrystallisation of **N23** in the presence of excess tetrabutylammonium tetrafluoroborate as electrolyte. This is the first reported structure for any salt of **N23**$^{+\bullet}$, and neither are any salts of the analogous Se$_2$ or Te$_2$ cations known. After exhaustive trials, each lasting for multiple weeks during the slow growth of crystals on the working electrodes from necessarily dilute solutions, only a few very well-defined crystals could be harvested, and recrystallization was impossible. The major emphasis in characterization was to obtain SC-XRD. There was insufficient sample for a magnetic or EPR characterization (noting that structures of this type are typically bulk diamagnets with some LT paramagnetism from defect sites in their lattices).[78] The cation radicals organize into sets of distinct in-register dimers and interact with the ordered BF$_4^-$ anions through a network of stronger and weaker

21

intermolecular contacts, predominantly between F and S atoms (Fig. 7). The mean interplanar spacing (C-C bond midpoint to centroid of C3S2 ring) within these three dimers is 3.160(16) Å, considerably shorter than $\sum r_{vdW}(C+S) = 3.50$ Å, and 6.9% less than the π-stacking separation (central C atom to centroid of C6 ring below) of 3.393 Å in the structure reported for neutral **N23** (CSD refcode: DAQMUE).[31] These features are fully consistent with the description of *pancake-bonded dimers* in [**N23**]BF$_4$.[78-80] An analogy with other S$_2$-containing radicals may be found in both neutral [1,2,3,5-dithiadiazolyl]$_2$ dimers,[81] and especially in salts of pancake-bonded [S$_3$N$_2^+$]$_2$ dimers.[82]
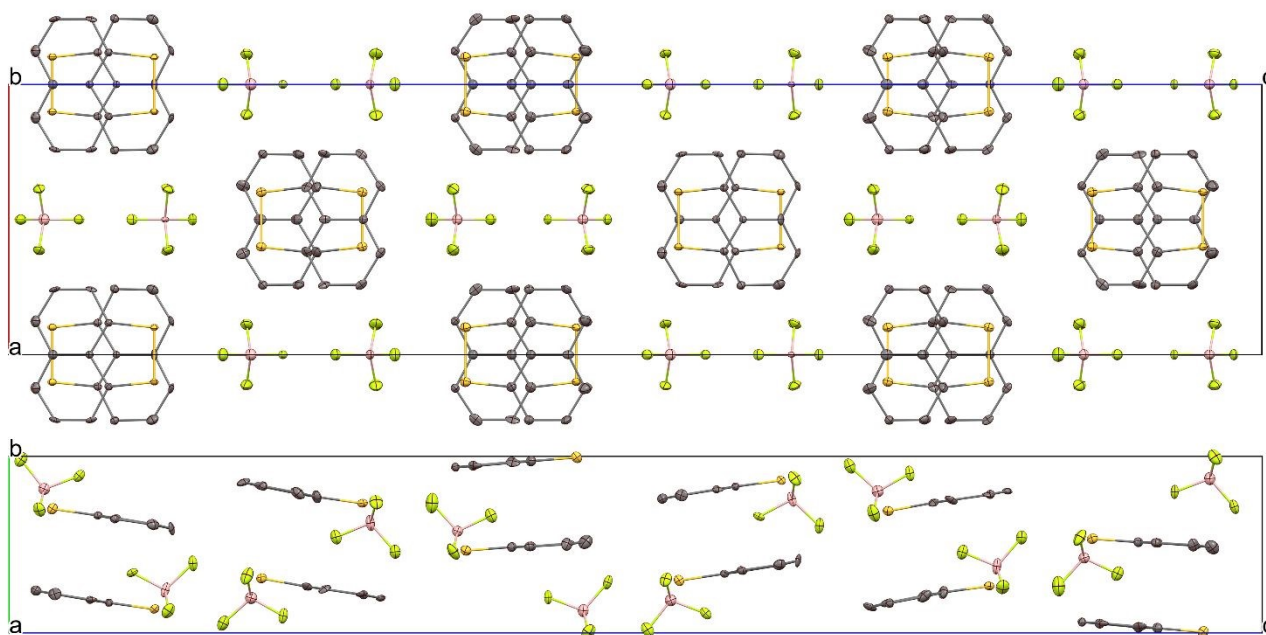
Fig. 8. Unit cell packing diagrams of naphtho[1,8-*cd*]-1,2-dithiolium tetrafluoroborate [**N23**]BF$_4$: (top) projection down the *b* crystallographic axis; (bottom) projection down *a*. H atoms omitted for clarity. The [2 0 0] mirror planes bisect the dimers of cations and the anions; dimers in the upper/lower and middle registers (top view) are related to each other by 2$_1$ screw axes parallel to the *c* axis at ¼*a*,½*b* and ¾*a*,½*b*.

The structure of [**N23**]BF$_4$ solves in the orthorhombic space group *Pnm*2$_1$ with *Z'* = 4. The overall structure of the lattice is highly ordered, and both the cation radicals and the anions are bisected by [2 0 0] mirror planes (i.e. ⊥ to the *a* axis at both the cell edges and middle – see Fig. 8). Horizontal 2$_1$ screw axes parallel to *c* organize the in- and out-of-register orientations of cations and anions as is clear from the top and side views in Fig. 8.

The average S–S distance in the six cation radicals in this crystal structure is 2.046(5) Å, which may be compared to a mean of 2.092(2) Å from the two independent molecules in neutral **N23**,[31] i.e. just 2.0 % shorter upon one-electron oxidation. To better understand these differences in %-bond shortening compared to the much larger changes computed for the di(phenylsulfur) analogues **N7** and **A1**, B3LYPD3(BJ)/6-31+G(d)/PCM(CH$_2$Cl$_2$) DFT calculations were undertaken on **N23**, **N23**$^{+\bullet}$ and **N23**$^{+2}$ (Table 3 and Fig. 9). The one-electron oxidation that results in the electrocrystallisation of [**N23**]BF$_4$ is therefore expected to remove a single electron from the HOMO, which is a highly-delocalized π orbital that includes the two S *p* orbitals but also eight of the ten C atoms of the naphthalene ring (the central C atoms are located

at a vertical nodal plane) and is formally π-antibonding w.r.t the S–S bond. The computed S–S distances are 2.137, 2.086 and 2.055 Å in **23**, **23**[+•] and **23**[+2], respectively, which corresponds to a 2.4% reduction between neutral and cation radical, in excellent agreement with experiment.
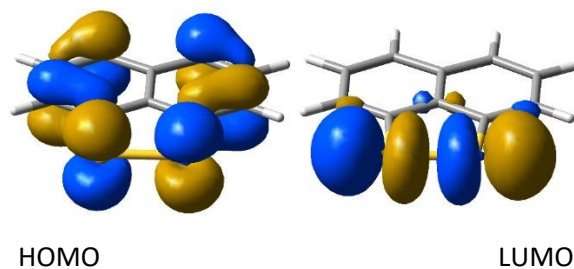

| HOMO | LUMO |

Fig. 9. Kohn-Sharm orbital surfaces from B3LYPD3(BJ)/6-31+G(d) calculations on **23** showing the two RMOs.

The face to face (but head to tail) dimers observed in the crystal structure of [**N23**]BF$_4$ (Fig. 7), correspond to the strongly preferred maximum overlap orientation of radical SOMOs, a noted feature of pancake bonding. To demonstrate this better, a DFT calculation using our standard method (but without solvation) was undertaken on a static dimer structure using one of the closely spaced [**N23**]$_2$[2+] units excised from the SC-XRD structure (Fig. 10). The HOMO clearly shows the in-register overlap of the ring C and S p-orbitals that constitute the SOMO of the monomer (compare Fig. 10 and the ESI). By contrast, in neutral **N23**, along with the typical π-stacking separation, the π-HOMO and HOMO-1 are distinctly out-of-register and instead the typical graphitic 'C-over-ring-centroid' structure is adopted (for a DFT calculation, see the ESI).[75]
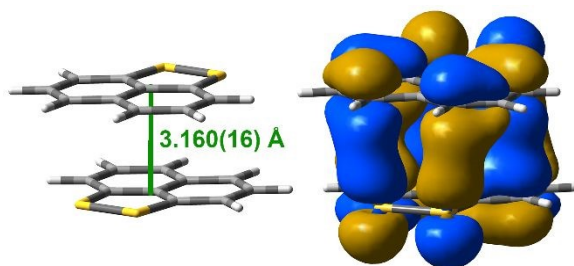

3.160(16) Å

Fig. 10. B3LYP-D3(BJ)/6-31+G(d) calculated dimer structure for [(**N23**)]$_2$[2+]. (Left) the geometry from SC-XRD with mean interplanar spacing indicated; (right) Kohn-Sham orbital surface with isovalue of 0.02 showing the in-register overlap of the p-AOs of the SOMOs of the constituent monomer radicals.

Pancake bonding represents a challenging case for intermolecular bonding, with typical features of interaction distances considerably shorter than van der Waals contact distances, multireference singlet ground states, and concurrently important dispersion interactions.[73, 78-84] This is further complicated in [**N23**]BF$_4$ by the large coulombic charges amongst the cation radicals and BF$_4^-$ counterions. The only charged radicals for which the energy of pancake bonding has been quantified, to our knowledge, is for dimers of anion radicals of tetracyanoethene (TCNE), which have been extensively investigated.[83,84] For the specific case of the salt K$_2$TCNE$_2$, Mou *et al.* have carefully validated a series of DFT functionals (including B3LYP-D3(BJ)) that are capable of reproducing the energy of the pancake bonding interaction obtained from multireference averaged coupled cluster wavefunction methods (–42.3 kJ/mol).[83,84] In order to minimize the Coulombic contributions to the energy, they created a model structure where two K$^+$ ions occur in the lattice

above and below a $[TCNE_2]^{-2}$ dimer, effectively isolating the charge compensation of the ion-pairing from the inter-radical anion bonding. We have undertaken a similar approach to that described by by Mou et al.,[84] by calculating a comparison of the energies of such charge-compensated ion pair 'dimers' $[(N23)BF_4]_2$ (by gas-phase optimization of both 'equatorial' and 'axial' models, as done for K_2TCNE_2; see the ESI for a description and results) with that in which the two constituent $[(N23)BF_4]^{\bullet}$ radical ion pairs are separated perpendicularly to 10.0 Å, a distance shown to significantly exceed the cut-off of any pancake interaction (no sensible closed-shell structure could be located, and these separated radical ions are well described by a triplet wavefunction, see the ESI for details).[83,84] The energy of the interaction estimated by such an approach for the axial model is −99 kJ/mol (separated triplet vs. bound singlet), which is far too large compared to typical values for pancake bonding between small radical monomers (−29 to −48 kJ/mol).[78,80] This dimer has a closed-shell singlet electronic structure (with a sizeable HOMO-LUMO gap of 2.0 eV, a triplet state that optimizes 50 kJ/mol higher in energy, and no open-shell singlet that could be found using a broken-symmetry approach). The high interaction energy is probably acerbated by basis-set superposition error. However, in the absence of high-level wavefunction calculations such as are available for K_2TCNE_2, and in view of strong evidence that DFT methods need prior validation before they can be trusted to give reliable interaction energies,[84] the above should be taken as only a preliminary estimate. Thus, whilst pancake bonding is clearly recognizable in the $[N23]BF_4$ crystal structure, a reliable determination of the energy of the radical-radical interaction is outside the scope of this work.

Discussion

Electron transfer mechanisms (ETM). The naphtho-[1,8-*cd*][1,2]dichalcogenoles, Type I in Chart 1, are comparatively simple to discuss, so their ETMs will be developed first. For the specific case of **N23** (Scheme 2, $E_1=E_2=S$) a detailed electrochemical investigation has been reported in conjunction with the observation of film formation on electrodes when oxidation is extended to a second, chemically irreversible, oxidation process.[49] Scheme 2 presents a simplified version of the ETM proposed by Sarukawa and Oyama; their original also identified the C_2 and C_4 sites of the dication as potential sites for dimerization/oligomerization.[49] In addition, a reversible reduction to an anion radical and irreversible reduction to a dianion is included, based on their exhaustive voltammetric investigation. The available voltammetric data for this class with the other chalcogens suggests that a similar mechanism may operate for the remaining derivatives, but the limited evidence precludes a firm conclusion.
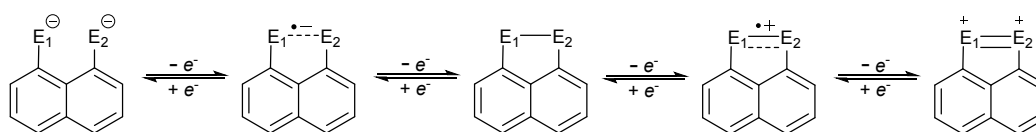
Scheme 2. ETM for *peri*-disubstituted naphtho-[1,8-*cd*][1,2]dichalcogenoles.

The results presented in this work now allow for an unambiguous assignment of an ETM for anodic processes in the Type II compounds. Specifically, that the oxidative voltammetry of **A1** − **N12** results in the

formation of a radical cation after $1e$ and a diamagnetic dication after $2e$ transfer, and that both processes are chemically reversible and electrochemically *quasi*-reversible (Scheme 3a). This has been further confirmed by the isolation of crystals of the radical cation hemi-bonded salts [53,54] and crystals of salts of dications consistent with a $2e$ bond between E_1 and E_2 (E = S, Se, Te).[51] What the CVs in Fig. 1 demonstrate is that oxidation is energetically much easier for Te > Se > S, and furthermore that the *separation* in energies, given by the potential difference ΔE_{2-1}, decreases dramatically in the sequence Te << Se < S. This indicates a very strong chalcogen control over the redox processes. Consistent with this is that isolated salts of the radical cation have only been reported when $E_1 = E_2 = S$ or Se, whilst only salts of the dications have been obtained when $E_1 = E_2 = Te$. The potentials for the first and second e transfer in the case of Te are energetically too close for isolation of the radical cation and disproportionation to neutral and dication will always occur for sub-stoichiometric reactions.
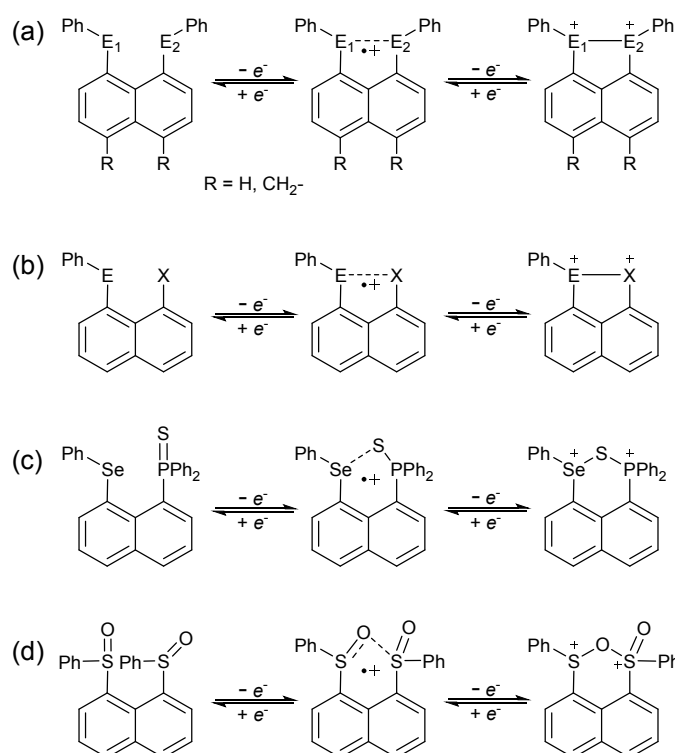
Scheme 3. ETMs for oxidation of *peri*-disubstituted diaryl dichalcogenides **A1 – N12** to form new bonds.

Similar bond-forming anodic electrochemistry probably applies for **N13 – N16** (Scheme 3b) although no oxidized products have been isolated to our knowledge. For **N17** (Scheme 3c) and **N18** (Scheme 3d) the proposed interpretations depend heavily on the DFT computational evidence presented in the ESI, and is structurally corroborated only by the isolation of the neutral acenaphthene C_3Te_2O ring in WARPIQ.[26]

Structural aspects: consequences of electron transfer in peri-substituted naphthalenes A1-N18 and N23.
Extensive DFT computational calculations were necessary to establish a series-wide correlation between the solution voltammetry E_p^{a1} data and adiabatic ionisation energies. A convincingly linear trend could be established (Fig. 11) although the data show some scatter (R^2 = 0.88). The mixed tellurium/halogen species **N15** and **N16** are the worst outliers, which may reflect either computational limitations (of the theoretical

level with only quasi-relativistic treatment of the very heavy elements through pseudopotentials (Te, I), possibly also with wrong predictions of the preferred conformations in solution) or experimental (indicated by a greater dependency of the measured potentials on the type of working electrode), or both. The WBI value of 0.737 for **N15**$^{2+}$ is one of the largest values amongst this set, consistent with a 2e dative single bond from I to Te in this putative dication. Indeed, in view of the uncertainties in assigning the correct solution conformations by DFT from limitations in the D3(BJ) dispersion corrections, the calculated AIP data should be assigned an uncertainty of no less than ±0.1 eV. The experimental uncertainty between separate experiments is ±0.1 V.
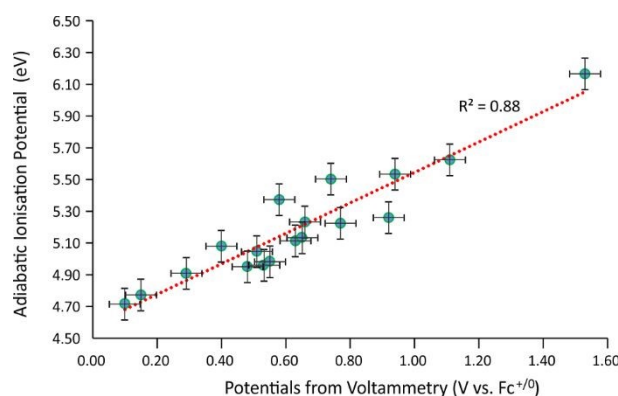

Fig. 11. Correlations between DFT computed ionisation energies for **A1** – **18** with the E_p^{a1} data from solution voltammetry at a Pt electrode. The estimated errors in AIP and voltammetric potentials are indicated.

Mechanistic aspects: conformational analysis. As mentioned in Results, the voltammetric data attest to uniformly *quasi*-reversible e transfer in both oxidation processes, which in molecular systems such as these, usually indicates a change in conformation after e transfer. Obviously, the uncertainty in predicting the true lowest-energy solution conformations in each charge state discussed above will also affect any attempts to correlate geometry changes to e transfer. However, it is clear, from both computational results (Table 3) and from the structures of isolated salts, that there are large structural changes upon oxidation, with shortening of the E···E distances by as much as 33% for the Type II compounds. This is much greater than for chemically bonded atoms, for example in the Type I exemplar **N23**, for which shortening of 2% in the first and 4% (overall) in the second electron transfer is predicted. Thus, electron transfer in the Type II compounds is systematically associated with large geometrical changes and the slowed rates of electron transfer are not surprising. On the other hand, the reliable two-step chemical reversibility of this series (because the associated RMOs are localized at the chalcogens) is in strong contrast to that of **N23**, which is subject to electropolymerization upon the second e transfer (because the RMO is delocalized over chalcogen and ring C atoms).[49]

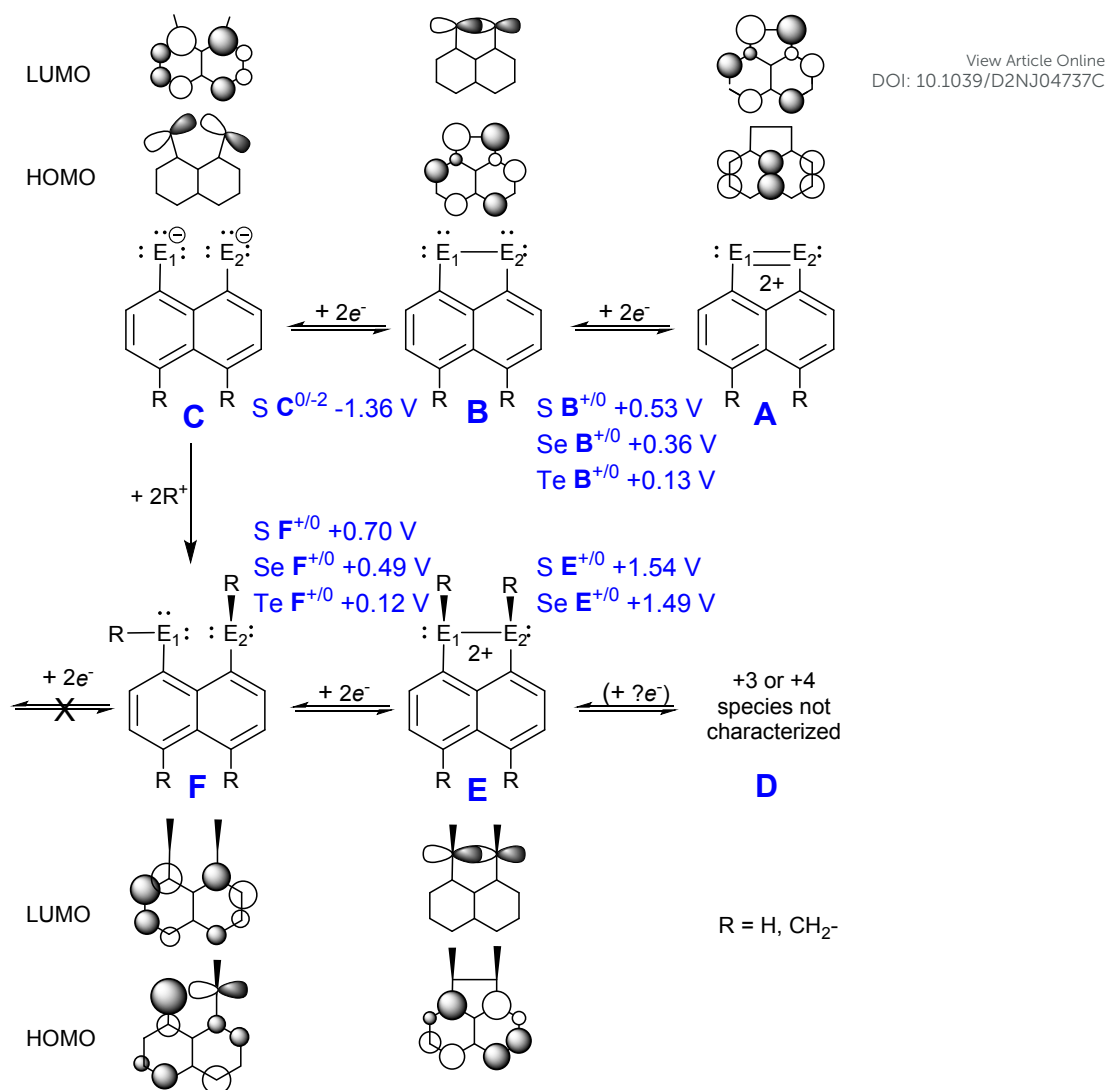Chalcogen controlled redox behaviour in peri-substituted S, Se and Te naphthalene derivatives

Fig. 12. Comparative RMOs of the Type I and Type II dichalcogen naphthalene/acenaphthenes correlated to the redox transformations, expressed as standard reductions for the putative 2*e* transformations.

Electronic structure correlation to voltammetry for Type I and II systems. The combined experimental and computational investigation reported in this work, in conjunction with extant data from the longer-investigated Type I species, enable us to put forward an integrated interpretative framework for the observed redox transformations for these related sets of compounds (see Fig. 12).

For simplicity, the interpretation in Fig. 12 is presented in 2*e* steps (i.e. correlated with the occupancies of the associated RMOs) and as formal electrochemical reductions, the standard approach in electrochemistry. Thus, for example, the formal reduction of Type I dication **A** to neutral **B** is not feasible in practice (due to reactivity of **A** towards polymerization or oligomerization)[49] but is conceptually useful. Similarly, 2*e* reduction of **B** leads to dianion **C**, which on DFT optimization is highly distorted, and whose existence in chemical reduction probably depends on stabilization by coordination to cations, but the HOMO topology is obviously a (distorted) version of the LUMO of **A**. Type I and II rings are related (conceptually) by trapping of this dianion by two R⁺ groups. The AB conformation of neutral **F** results in far less out-of-plane distortions of the $C_{10}E_2$ moiety than in **C** because neutral **F** has rotated one of the chalcogen *p* orbitals

contributing to the HOMO by almost 90°. In the Type II dication **E** the RMOs, whether adopting AA*c* or AA*t* conformations, return to being isolobal with those of neutral **B**, albeit with a shift in occupancy for the HOMO from the chalcogens into the aromatic rings. In that regard, it is very much to be expected that any further oxidation (e.g. to radical cation **D**[+•]) will highly activate the napthalenic ring for radical coupling or polymerization, in full agreement with the experimental observation of fully chemically irreversible processes above +1.5 V vs. $Fc^{+/0}$ (see Results).

Fig. 12 also shows the potentials (as E_m where available) for the first couples, e.g. **B**[+/0] to indicate the relative energies for the transformations. The 'neutralization' afforded by the conceptual trapping of dianion **C** by the two R[+] naturally re-sets the redox energies, such that the **F**[+/0] couples are comparable to, and indeed slightly higher, than **B**[+/0]. Similarly, the reduction potentials for **F** are shifted (in the negative direction) out of experimental range. More significantly, the voltage dependence with chalcogen type of the **F**[+/0] couples is about 50% larger than for **B**[+/0]. This reflects the stronger destabilization in HOMO energies in **F** compared to **B**, a direct consequence of the non-bonded *peri*-interactions. Whilst still fully correlated with the expected element dependencies (Te < Se <S) for both series, the amplified effect of the element sizes when constrained to the close non-bonded *peri*-distances stands out for Type II. The experimental evidence for an exceptional degree of chalcogen control over redox behaviour in these systems is thus fully rationalized by their RMO energies and topologies.

Experimental Section

Reagents and General Procedures. Dichloromethane (BDH, reagent grade) was purified by distillation from CaH_2 and purged with dry argon prior to use. Electrochemical grade tetrabutylammonium hexafluorophosphate [$^nBu_4N$][PF_6] (Fluka) was used as the supporting electrolyte and was stored in a desiccator. Ferrocene (Fc) was sublimed prior to use. Substrates **A1 – N18** were prepared as previously described.[7,9,11,59,62-64] **N23** was prepared according to the literature method.[9]

Voltammetry. Cyclic voltammograms (CV) were obtained at 21 ± 2°C in CH_2Cl_2 containing 0.4 M [$^nBu_4N$][PF_6] as the supporting electrolyte. Solutions were purged with dry argon for 10 min directly before use and were kept under a blanket of argon during all experiments. CV measurements were performed with a Princeton Applied Research PARSTAT 2273 potentiostat. The voltammetry cell has been described previously.[85] Initial background scans characterized the size of the accessible electrochemical window and provided estimates of the likely background currents. The CVs were obtained over scan rates of 0.1 – 10 V s^{-1}. Potentials for compounds **A1 – N18** are reported versus the operative formal potential for the Fc[+/0] redox couple, which was used as an internal standard.[86] The working electrodes were either a 3.0 mm BASi GC or a 1.6 mm BASi Pt, and these were polished with an Al_2O_3 (Buehler, 0.05 μm) slurry on a clean polishing cloth, rinsed with distilled water, and dried with tissue paper prior to use. All compounds were fairly soluble in CH_2Cl_2 to give clear to yellow-coloured solutions. In the case of **A1-N12** there were three oxidation processes

evident and no reduction processes up to the solvent electrolyte limit (−2.4 V). Broadly similar responses were seen for all 18 compounds at both the GC and Pt working electrodes.

EPR and SEEPR. SEEPR was undertaken under control of a BASi potentiostat.[85] EPR spectra were obtained with a Bruker EMX 10/12 spectrometer operating at ~9.7 GHz with 100 kHz modulation. Simultaneous electrochemical/electron paramagnetic resonance (SEEPR) spectroscopy experiments were undertaken in the previously described *in situ* EPR electrochemical cell, a 5 mm wide quartz EPR flat cell containing a gold-foil electrode stabilized in a laminated plastic film, with a Teflon-coated Ag wire reference and Teflon-coated Pt wire counter electrode.[85] Square wave voltammograms (SWV) are run initially to identify signals to the first $1e$ transfer as discussed above, i.e. slightly positive of E_p^{a1}. Typically, a 60 s electrolysis is undertaken in conjunction with an EPR scan of the same duration through a region of magnetic field that will bring the full spectrum within resonance. Strong EPR signals are generated within a few seconds of commencing electrolysis.

EPR spectra on **A1**–**A6** were undertaken at University of St Andrews. Samples were prepared under nitrogen and contained in 4 mm OD quartz tubes (Wilmad lab-glass) sealed with rubber septa (Sigma-Aldrich). Spectra of **A1**$^{+\bullet}$ were recorded using an 8 mT field sweep centred at 347.5 mT with 2048 points resolution, a time constant and conversion time of 40.96 ms each, a modulation amplitude of 5 µT and a microwave frequency of 9.7510 GHz. To resolve as many hyperfine lines as possible, 100 scans were accumulated. The field offset was calibrated with DPPH.

DFT Computational Methods. A wide range of geometries were optimised for both monocationic and dicationic dichalcogen diphenyl derivatives (Scheme 3) in the gas phase using the well-known B3LYP functional [87,88] with use of Curtis and Binning's 962(d) basis set [89] on Se and Br, the Stuttgart-Dresden effective core potential [90] applied to Te and I (augmented with d-polarisation functions with exponents of 0.237 and 0.266, respectively) [90] whilst the 6-31+G(d) basis set was applied to all other atoms (carbon, hydrogen, oxygen and sulfur). Minimum geometries were verified using harmonic vibrational analysis. The use of Grimme's D3 correction for dispersion, an attractive effect which is not readily accounted for by the bare B3LYP functional, along with Becke-Johnson damping,[91,92] denoted D3(BJ) was shown to be essential to generate structures that approximate to those obtained experimentally by SC-XRD.[93-95] Additionally, the effect of solvation has been approximated using a polarisable continuum model (PCM) for dichloromethane (ε = 8.93), the solvent employed in the voltammetry studies, to assess the effect of solvent polarity on preferred conformers and thus the adiabatic ionisation potential.[96,97] Bonding character between any pair of atomic centres may be readily assessed by evaluating the Wiberg Bond Index (WBI) using Natural Bond Orbitals.[98] In the WBI method, a value approaching 1 denotes a single bond with higher values denoting increasingly large bond orders and lesser values a weaker interaction. Adiabatic ionisation potentials were computed for both the first and second oxidations. Significantly, the adiabatic IPs are significantly damped in this (weakly coordinating) solvent, though the values remain large (~5 eV) compared to the solution values from voltammetry of at most a few volts. Incorporation of the solvation model has the most dramatic effect on

the AIP[2], reducing almost in half from the gas phase values and indicating the very large stabilization of the doubly charged ion in solution. All calculations reported in the main article were done with Gaussian 16W on Intel CORE i7-8700 PCs under Windows 10.[99]

Crystallography. Details of the crystallographic structure determinations for **A19 – A22** and [**N23**]BF$_4$ are summarized in Table 5 and provided in detail in the ESI. Archival structural data have been deposited under Acquisition Codes 2205312-2205316 These data can be obtained free of charge from The Cambridge Crystallographic Data Centre via their website at www.ccdc.cam.ac.uk/data_request/cif. Data analysis was performed, and illustrations prepared, with Mercury CSD 2022.2.[100]

Electrocrystallisation, [S$_2$C$_{10}$H$_6$][BF$_4$]. 10 mL of a 0.15 M tetrabutylammonium tetrafluoroborate salt solution (0.494 g) in 1,1,2-trichloroethane (TCE) and 5 mL of a 1.2 x 10^{-2} M solution of naphtho[1,8-*cd*]-1,2-dithiole in 1,1,2-trichloroethane were prepared. 5 mL of the naphtho[1,8-*cd*]-1,2-dithiole solution was added to the anode compartment of a glass H-cell (containing a fine porosity glass frit between the two compartments and two Pt wire electrodes) and 5 mL of the tetrabutylammonium tetrafluoroborate was added to the cathode compartment. The remaining 5 mL of the tetrabutylammonium tetrafluoroborate solution was added in equal amounts to the anode and cathode compartments to produce equal solution heights on both sides. Both solutions were purged for 30 seconds with nitrogen and the Pt electrodes were placed in their respective compartments and adjusted in height so that they were immersed in the solutions but not touching the bottom. The apparatus was covered in aluminium foil to exclude light, and the current was adjusted to 3 μA. After four weeks the crystals were harvested. This was done by carefully lifting the anode from the solution and brushing the crystals onto a suction filter where they were washed with some cold TCE and dried under vacuum. The resulting crystals were suitable for SC-XRD. The yield was insufficient to perform further chemical characterization, but all the crystals harvested had identical diffraction patterns.

Table 5. Crystallographic data collection and refinement parameters for crystal structures **A19** - [**N23**]BF$_4$

Parameter	A19	A20	A21	A22	[N23]BF$_4$
Formula	C$_{25}$H$_{23}$BF$_4$O$_2$STe	C$_{26}$H$_{25}$BF$_4$O$_2$SeTe	C$_{26}$H$_{26}$BF$_4$O$_2$Te$_2$	C$_{48}$H$_{36}$B$_2$F$_8$OSe$_2$Te$_2$· 1.7CH$_2$Cl$_2$	C$_{10}$H$_6$BF$_4$S$_2$
FW (g/mol)	601.92	662.85	712.49	1359.91	277.08
Temp. (K)	125	125	93	93	93.1
Cryst syst	triclinic	triclinic	triclinic	monoclinic	orthorhombic
Space Grp	$P\bar{1}$	$P\bar{1}$	$P\bar{1}$	$P2_1/n$	$Pmn2_1$
A (Å)	11.7625(19)	10.415(8)	10.593(3)	12.1170(2)	10.117(2)
b (Å)	14.973(4)	11.443(6)	11.100(2)	19.875(3)	6.607(2)
c (Å)	15.390(3)	11.777(6)	12.010(2)	20.939(2)	46.904(9)
A (°)	83.26(3)	61.44(3)	61.571(14)	90	90
β (°)	71.08(2)	84.01(4)	85.183(18)	95.196(15)	90
γ (°)	68.25(2)	88.75(4)	87.92(2)	90	90
Volume (Å^3)	2381.4(10)	1225.4(13)	1237.4(5)	5021.9(8)	3135.3(9)
Z	4	2	2	4	12
Z'	2	1	1	1	3
R$_1^a$ [I ≥ 2σ(I)]	0.0758	0.0680	0.0345	0.0781	0.0698
wR$_2$ [all data]	0.1724	0.2161	0.0576	0.2312	0.1614
CCDC	2205312	2205313	2205314	2205315	2205316

Conclusions

In the voltammetric analysis of Type II *peri*-disubstituted naphthalene frameworks substituted by either halogens or PhE (E = S, Se or Te) moieties, there is clear evidence that the ease of oxidation is strongly controlled by the nature of the chalcogen atoms E. Our comprehensive computational investigation has surveyed all possible conformational combinations of the two Ph groups per molecule and has demonstrated that *peri*-interactions induce specific ground state structural preferences. Despite such energy-minimising choices, it is evident from the computed HOMO energies that the unfavourable interactions of such tightly spaced neutral atoms raises the energies of these non-bonded electrons and thus significantly favours oxidation. This destabilization systematically increases from S to Se to Te. The mono- and doubly oxidized products, by contrast, develop substantial E$\cdots$E bonding character. This has been predicted via computed Wiberg bond indices and confirmed from d(E$\cdots$E) measurements in crystal structures of their salts.

The chemical reactivity of the oxidized states demonstrates a strong susceptibility towards nucleophilic attack. By contrast, the electrosynthetic production of Type I derivative [**N23**]BF$_4$, the first reported structure for any salt of this type, provides an elegant example of pancake bonded dimers of radical cations within a crystalline solid, in which the inter-ring separation shortens three times more than does the S–S bond distance upon 1e oxidation. A robust RMO-based interpretation that links the redox behaviour of Types I and II has been developed. Future work in this area would be greatly enhanced by a comprehensive voltammetric investigation of the redox processes for the already long-known Type I chalcogen derivatives, all of which are accessible by reliable synthetic strategies. The importance of this class to materials chemistry provides a clear rationale for undertaking such a study.

Acknowledgements

References

1.   A. Gehlhaar, C. Wölper, F. van der Vight, G. Jansen and S. Schulz, *Eur. J. Inorg. Chem.*, 2021, e202100883:1-9. DOI: 10.1002/ejic.202100883.

2.   S. Hayashi, M. Uegaito, T. Nishide, E. Tanaka, W. Nakanishi, T. Sasamori, N. Tokitoh and M. Minoura, *New J. Chem.*, 2019, **43**, 14224. DOI: 10.1039/c9nj02198a.

3.   S. Hayashi, K. Matsuiwa, H. Miza, and W. Nakanishi, *Heteroatom Chem.* 2014, **25**, 449. DOI: 10.1002/hc

4.   R. S. Glass, *Top. Curr. Chem.*, 2018, **376**, 22. DOI: 10.1007/s41061-018-0197-0

5.   W. Wang, Z. Sun, L. Meng, and X. Li, *Int. J. Quantum Chem.*, 2016, **116**, 1090. DOI: 10.1002/qua.25143.

6.   G. Sánchez–Sanz, I. Alkorta and J. Elguero, *Molecules*, 2017, **22**, 227. DOI: 10.3390/molecules22020227.

7.   S. Hayashi, W. Nakanishi, A. Furuta, J. Drabowicz, T. Sasamoric and N. Tokitoh, *New J. Chem.*, 2009, **33**, 196. DOI: 10.1039/b809763a.

8.   W. Nakanishi, S. Hayashi, and S. Toyota, *J. Org. Chem.* 1998, **23**, 8790. DOI: 10.1021/jo980885l.

9.   P. Nagy, D. Szabó, I. Kapovits, A. Kucsman, G. Argay and A. Kálmán, *J. Mol. Struct.*, 2002, **606**, 61. DOI:

10. H. Fujihara, M. Yabe, J-J. Chiu and N. Furukawa, *Tetrahedron Lett.* 1991, **32**, 4345. DOI:

11. H. Fujihara, H. Ishitani, Y. Takaguchi and N. Furukawa, *Chem. Lett*. 1995, 572. DOI:

12. R. S. Glass, *Top. Curr. Chem.* 1999, **205**, 1. DOI:

13. R. Weiss, E. Aubert, P. Pale and V. Mamane, *Ange. Chem. Int. Ed.*, 2021, 19281. DOI: 10.1002/anie.202105482.

14. B. Zhou and F. P. Gabbai, *Organometallics*, 2021, **40**, 2371. DOI: 10.1021/acs.organomet.1c00279.

15. M. Baba and T. Mizuta, *Polyhedron*, 2015, **92**, 30. DOI: 10.1016/j.poly.2015.02.023.

16. K. S. Athukorala Arachchige, L. M. Diamond, F. R. Knight, M-L. Lechner, A. M. Z. Slawin, and J. D. Woollins, *Organometallics*, 2014, **33**, 6089. DOI: 10.1021/om500755w.

17. L. M. Diamond, F. R. Knight, K. S. Athukorala Arachchige, R. A. M. Randall, M. Bühl, A. M. Z. Slawin, and J. D. Woollins, *Eur. J. Inorg. Chem.*, 2014, 1512. DOI: 10.1002/ejic.201301549.

18. C. Kirst, B. E. Bode, D. B. Cordes, P. S. Nejman, A. M. Z. Slawin, K. Karaghiosoff and J. D. Woollins, *Dalton Trans.* 2016, **45**, 6348. DOI: 10.1039/c6dt00304d.

19. A. Nordheider, E. Hupf, B. A. Chalmers, F. R. Knight, M. Bühl, S. Mebs, L. Chęcińska, E. Lork, P. Sanz Camacho, S. E. Ashbrook, K. S. Athukorala Arachchige, D. B. Cordes, A. M. Z. Slawin, J. Beckmann and J. Derek Woollins, *Inorg. Chem.* 2015, **54**, 2435. DOI: 10.1021/ic503056z.

20. M. W. Stanford, F. R. Knight, K. S. Athukorala Arachchige, P. Sanz Camacho, S. E. Ashbrook, M. Bühl, A. M. Z. Slawin and J. D. Woollins, *Dalton Trans.*, 2014, **43**, 6548. DOI: 10.1039/c4dt00408f.

21. M. Bühl, F. R. Knight, A. Křístková, I. Malkin Ondík, O. L. Malkina, R. A. M. Randall, A. M. Z. Slawin, and J. D. Woollins, *Angew. Chem. Int. Ed.*, 2013, **52**, 2495. DOI: 10.1002/anie.201205998.

22. J. M. Griffin, F. R. Knight, G. Hua, J. S. Ferrara, S. W. L. Hogan, J. D. Woollins and S. E. Ashbrook, *J. Phys. Chem. C*, 2011, **115**, 10859. DOI: 10.1021/jp202550f.

23. L. J. Taylor, M. Bühl, B. A. Chalmers, M. J. Ray, P. Wawrzyniak, J. C. Walton, D. B. Cordes, A. M. Z. Slawin, J. D. Woollins, and P. Kilian, *J. Am. Chem. Soc.*, 2017, **139**, 18545. DOI: 10.1021/jacs.7b08682.

24. P. S. Nejman, B. Morton-Fernandez, N. Black, D. B. Cordes, A. M.Z. Slawin, P. Kilian, J. D. Woollins, *J. Organomet. Chem.*, 2015, **776**, 7. DOI: 10.1016/j.jorganchem.2014.10.023.

25. C. G. M. Benson, C. M. Schofield, R. A. M. Randall, L. Wakefield, F. R. Knight, A. M. Z. Slawin, and J. D. Woollins, *Eur. J. Inorg. Chem.*, 2013, 427. DOI: 10.1002/ejic.201200967.

26. F. R. Knight, K. S. Athukorala Arachchige, R. A. M. Randall, M. Bühl, A. M. Z. Slawin and J. D. Woollins, *Dalton Trans.*, 2012, **41**, 3154. DOI: 10.1039/c2dt12031c.

27. R. E. Sioda and B. Frankowska, *J. Electroanal. Chem.*, 2008, **612**, 147. DOI: 10.1016/j.jelechem.2007.07.016.

28. D. G. Gray, *An investigation of electoanalytical techniques applicable to electrolytic polymerizations*, PhD Thesis, 1968 (University of Manitoba, Canada).

29. P. Kilian, F. R. Knight and J. D. Woollins, *Coord. Chem. Rev.*, 2011, **255**, 1387. DOI: 10.1016/j.ccr.2011.01.015.

30. P. Kilian, F. R. Knight and J. D. Woollins, *Chem. Eur. J.*, 2011, **17**, 2302. DOI: 10.1002/chem.201001750.

31. S. M. Aucott, H. L. Milton, S. D. Robertson, A. M. Z. Slawin and J. D. Woollins, *Heteroatom Chem.*, 2004, **15**, 530. DOI: 10.1002/hc.20055.

32. T. Kodama, M. Kodani, K. Takimiya, Y. Aso, and T. Otsubo, *Heteroatom Chem.*, 2001, **12**, 287. DOI:

33. P. Sanz, M. Yáñez and O. Mó, *New J. Chem.*, 2002, **26**, 1747. DOI: 10.1039/b205601a.

34. J. C. Stark, R. Reed, L. A. Acampora, D. J. Sandman, S. Jansen, M. T. Jones and B. M. Foxman, *Organometallics*, 1984, **3**, 732. DOI:

35. B. K. Teo, F. Wudl, J. H. Marshall and A. Krugger, *J. Am. Chem.Soc.*, 1977, **99**, 2349.

36. B. K. Teo, F. Wudl, J. J. Hauser and A. Krugger, *J. Am. Chem. Soc.*, 1977, **99**, 4862.

37. B. K. Teo and P. A. Snyder-Robinson, *Inorg. Chem.*, 1978, **17**, 3489.

38. B. K. Teo and P. A. Snyder-Robinson, *J. Chem. Soc., Chem. Commun.*, 1979, 255.

39. B. K. Teo and P. A. Snyder-Robinson, *Inorg. Chem.*, 1979, **18**, 1490.

40. B. K. Teo and P. A. Snyder-Robinson, *Inorg. Chem.*, 1981, **20**, 4235.

41. B. K. Teo, V. Bakirtzis and P. A. Snyder-Robinson, *J. Am. Chem. Soc.*, 1983, **105**, 6330.

42. B. K. Teo and P. A. Snyder-Robinson, *Inorg. Chem.*, 1984, **23**, 32.

43. H. Bock, G. Brahlera, D. Dauplaiseb and J. Meinwald, *Chem. Ber.*, 1981, **114**, 2622.

44. K. Bandyopadhyay, M. Sastry, V. Paul, and K. Vijayamohanan, *Langmuir*, 1997, **13**, 866.

45. T. Inamasu, D. Yoshitoku, Y. Sumi-otorii, H. Tani and N. Ono, *J. Electrochem. Soc.*, 2003, **150**, A128. DOI: 10.1149/1.1525267.

46. L. Zhang, S. M. Fakhouri, F. Liu, J. C. Timmons, N. A. Ran and A. L. Briseno, *J. Mater. Chem.*, 2011, **21**, 1329. DOI: 10.1039/c0jm02522d.

47. W. Ji, S. Jing, Z. Liu, J. Shen, J. Ma, D. Zhu, D. Cao, L. Zheng and M. Yao, *Inorg. Chem.*, 2013, **52**, 5786. DOI: 10.1021/ic302628y.

48. D. J. Press, T. G. Back, T. C. Sutherland, *Tetrahedron Lett.*, 2012, **53**, 1603. DOI: 10.1016/j.tetlet.2012.01.068.

49. T. Sarukawa and N. Oyama, *J. Electronal. Chem.*, 2010, **647**, 204. DOI: 10.1016/j.jelechem.2010.06.002.

50. F. B. Bramwell, R. C. Haddon, F. Wudl, M. L. Kaplan, J. H. Marshall, *J. Am. Chem. Soc.*, 1978, **100**, 4612. DOI:

51. F. R. Knight, R. A. M. Randall, T. L. Roemmele, R. T. Boeré, B. E. Bode, L. Crawford, M. Bühl, A. M. Z. Slawin, and J. D. Woollins, *ChemPhysChem*, 2013, **14**, 3199. DOI: 10.1002/cphc.201300678.

52. The Cambridge Structural Database, C. R. Groom, I. J. Bruno, M. P. Lightfoot and S. C. Ward, *Acta Cryst.*, 2016, **B72**, 171. DOI: 10.1107/S2052520616003954.

New Journal of Chemistry Accepted Manuscript

53. S. Zhang, X. Wang, Y. Su and X. Wang, *J. Am. Chem. Soc.*, 2014, **136**, 14666. DOI: 10.1021/ja507918c.

54. S. Zhang, X. Wang, Y. Su, Y. Qui, Z. Zhang and X. Wang, *Nature Chem.*, 2014, **5**, 4127. DOI: 10.1038/ncomms5127.

55. J. F. Berry, *Acc. Chem. Res.*, 2016, **49**, 27. DOI: 10.1021/acs.accounts.5b00517.

56. M. Marín-Luna, I. Alkorta and J. Elguero, *Struct. Chem.*, 2016, **27**, 753. DOI: 10.1007/s11224-015-0617-5.

57. D. Wang and A. Fujii, *Chem. Sci.*, 2017, **8**, 2667. DOI: 10.1039/c6sc05361k.

58. N. G. Connelly and W. E. Geiger, *Chem. Rev.*, 1996, **96**, 877.

59. L. K. Aschenbach, F. R. Knight, R. A. M. Randall, D. B. Cordes, A. Baggott, M. Bühl, A. M. Z. Slawin and J. D. Woollins, *Dalton Trans.*, 2012, **41**, 3141. DOI: 10.1039/c1dt11697e.

60. S. Hayashi and W. Nakanishi, *Bull. Chem. Soc. Jpn.*, 2008, **81**, 1605. DOI: 10.1246/bcsj.81.1605.

61. S. M. Aucott, H. L. Milton, S. D. Robertson, A. M. Z. Slawin and J. D. Woollins, *Dalton Trans.*, 2004, 3347. DOI: 10.1039/B409700A.

62. F. R. Knight, A. L. Fuller, M. Bühl, A. M. Z. Slawin, and J. D. Woollins, *Chem. Eur. J.*, 2010, **16**, 7503. DOI: 10.1002/chem.200903523.

63. F. R. Knight, A. L. Fuller, M. Bühl, A. M. Z. Slawin, and J. D. Woollins, *Chem. Eur. J.*, 2010, **16**, 7605. DOI: 10.1002/chem.201000435.

64. F. R. Knight, A. L. Fuller, M. Bühl, A. M. Z. Slawin, and J. D. Woollins, *Chem. Eur. J.*, 2010, **16**, 7617. DOI: 10.1002/chem.201000454.

65. O. Mallow, M. A. Khanfar, M. Malischewski, P. Finke, M. Hesse, E. Lork, T. Augenstein, F. Breher, J. R. Harmer, N. V. Vasilieva, A. Zibarev, A. S. Bogomyakov, K. Seppelt and J. Beckmann, *Chem. Sci.*, 2015, **6**, 497. DOI: 10.1039/c4sc02964j.

66. A. Zweig and A. K. Hoffmann, *J. Org. Chem.*, 1965, **30**, 3997.

67. D. A. O'brian, D. R. Duling, Y. C. Fann, EPR Spectral Simulation for MS-Windows, 2000. National Institute of Environmental Health Sciences, NIH, USA.

68. M. Mantina, A. C. Chamberlin, R. Valero, C. J. Cramer, and D. G. Truhlar, *J. Phys. Chem. A*, 2009, **113**, 5806. DOI: 10.1021/jp8111556.

69. K. B. Wiberg, *Tetrahedron*, 1968, **24**, 1083.

70. A. L. Fuller, F. R. Knight, A. M. Z. Slawin and J. D. Woollins, *Acta Crystallogr., Sect. E:Struct. Rep. Online*, 2007, **63**, o3855. DOI:10.1107/S1600536807040627.

71. W. Yang, L. Zhang, D. Xiao, R. Feng, W. Wang, S. Pan, Y. Zhao, L. Zhao, G. Frenking, X. Wang, *Nat. Commun.*, 2020, **11**, 3441. DOI: 10.1038/s41467-020-17303-4.

72. R. Weiss, Y. Cornaton, H. Khartabil, L. Groslambert, E. Henon, P. Pale, J-P. Djukic, and V. Mamane, *ChemPlusChem*, 2022, **87**, e202100518:1-12. DOI: 10.1002/cplu.202100518.

73. R. T. Boeré, *ACS Omega*, 2018, **3**, 18170. DOI: 10.1021/acsomega.8b03211.

74. S. Grimme, A. Hansen, J. G. Brandenburg, C. Bannwarth, *Chem. Rev.*, 2016, **116**, 5105.

75. S. Hembacher, F. J. Giessibl, J. Mannhart and C. F. Quate, *PNAS*, 2003, **100**, 12539. DOI: 10.1073_pnas.2134173100.

76. F. R. Knight, R. A. M. Randall, K. S. Athukorala Arachchige, L. Wakefield, J. M. Griffin, S. E. Ashbrook, M. Bühl, A. M. Z. Slawin and J. D. Woollins, *Inorg. Chem.*, 2012, **51**, 11087. DOI: 10.1021/ic301627y.

77. F. R. Knight, A. L. Fuller, M. Bühl, A. M. Z. Slawin and J. D. Woollins, *Inorg. Chem.*, 2010, **49**, 7577. DOI: 10.1021/ic101086h.

78. K. E. Preuss, *Polyhedron*, 2014, **79**, 1.

79. R. S. Mulliken and W. B. Person, *Molecular Complexes: A Lecture and Reprint Volume*; John Wiley & Sons Inc.: New York, 1969, Chapter 16.

80. M. Kertesz, *Chem.-Eur. J.*, 2018, **25**, 400. DOI: 10.1002/chem.201802385.

81. H. Z. Beneberu, Y-H. Tian and M. Kertesz, *Phys. Chem. Chem. Phys.*, 2012, **14**, 10713.

82. T. Chivers and R. S. Laitinen, *Chalcogen-Nitrogen Chemistry* (updated edition); World Scientific: Singapore, 2022, p.88ff.

83. Z-h. Cui, H. Lischka, T. Mueller, F. Plasser and M. Kertesz, *ChemPhysChem*, 2014, **15**, 165. DOI: 10.1002/cphc.201300784

84. Z. Mou, Y-H. Tian and M. Kertesz, *Phys. Chem. Chem. Phys.*, 2017, **19**, 24761. DOI: 10.1039/c7cp04637e

85. R. T. Boeré, A. M. Bond, T. Chivers, S. W. Feldberg, T. L. Roemmele, *Inorg. Chem.*, 2007, **46**, 5596.

86. G. Gritzner and J. Kuta, *Pure Appl. Chem.*, 1984, **56**, 461.

87. A. D. Becke, *J. Chem. Phys.* **1993**, *98*, 5648.

88. C. Lee, W. Yang, R. G. Parr, *Phys. Rev. B.* **1988**, *37*, 785.

89. R. C. Binning, L. A. Curtiss, *J. Comp. Chem.* **1990**, *11*, 1206.

90. G. Igel-Mann, H. Stoll, H. Preuss, *Mol. Phys.* **1988**, *65*, 1321.

91. A. D. Becke and E. R. Johnson, *J. Chem. Phys.* **2005**, *122*, 154104.

92. E. R. Johnson, A. D. Becke, *J. Chem. Phys.* **2006**, *124*, 174104.

93. S. Grimme, J. Antony, S. Ehrlich, H. Krieg, *J. Chem. Phys.* **2010**, *132*, 154104.

94. J. Antony, S. Grimme, *Phys. Chem. Chem. Phys.* **2006**, *8*, 5287.

95. L. Goerigk, S. Grimme, *Phys. Chem. Chem. Phys.* **2011**, *13*, 6670.

96. B. Mennucci, J. Tomasi, *J. Chem. Phys.* **1997**, *106*, 5151.

97. J. Tomasi, B. Mennucci, E. Cancés, *J. Mol. Struct. Theochem* **1999**, *464*, 211.

98. E. D. Glendening, C. R. Landis, F. Weinhold, *WIREs Comput Mol Sci* **2012**, *2*, 1.

99. Gaussian 16, Revision C.01, M. J. Frisch, G. W. Trucks, H. B. Schlegel, G. E. Scuseria, M. A. Robb, J. R. Cheeseman, G. Scalmani, V. Barone, G. A. Petersson, H. Nakatsuji, X. Li, M. Caricato, A. V. Marenich, J. Bloino, B. G. Janesko, R. Gomperts, B. Mennucci, H. P. Hratchian, J. V. Ortiz, A. F. Izmaylov, J. L. Sonnenberg, D. Williams-Young, F. Ding, F. Lipparini, F. Egidi, J. Goings, B. Peng, A. Petrone, T. Henderson, D. Ranasinghe, V. G. Zakrzewski, J. Gao, N. Rega, G. Zheng, W. Liang, M. Hada, M. Ehara, K. Toyota, R. Fukuda, J. Hasegawa, M. Ishida, T. Nakajima, Y. Honda, O. Kitao, H. Nakai, T. Vreven, K.

Chalcogen controlled redox behaviour in peri-substituted S, Se and Te naphthalene derivatives

Throssell, J. A. Montgomery, Jr., J. E. Peralta, F. Ogliaro, M. J. Bearpark, J. J. Heyd, E. N. Brothers, K. N. Kudin, V. N. Staroverov, T. A. Keith, R. Kobayashi, J. Normand, K. Raghavachari, A. P. Rendell, J. C. Burant, S. S. Iyengar, J. Tomasi, M. Cossi, J. M. Millam, M. Klene, C. Adamo, R. Cammi, J. W. Ochterski, R. L. Martin, K. Morokuma, O. Farkas, J. B. Foresman, and D. J. Fox, Gaussian, Inc., Wallingford CT, 2016.

100.   C. F. Macrae, I. Sovago, S. J. Cottrell, P. T. A. Galek, P. McCabe, E. Pidcock, M. Platings, G. P. Shields, J. S. Stevens, M. Towler and P. A. Wood, J. Appl. Crystallogr., 2020, **53**, 226.